Thermal Science and Engineering Progress 73 (2026) 104642

Contents lists available at ScienceDirect

Thermal Science and Engineering Progress

journal homepage: www.sciencedirect.com/journal/thermal-science-and-engineering-progress

Assessment of Monel 400 corrosion in hydrofluoric–hydrochloric acid condensation environments for condensing heat exchangers

Vassilis Stathopoulos [a,*], Pavlos K. Pandis [a], Athanasios Zarkadoulas [a], Paraskevi Nanou [a], Dimitrios Fragkoulis [a], Robertas Poškas [b], Arūnas Sirvydas [b], Povilas Poškas [b], Jurgis Jankaukas [b], Hussam Jouhara [c]

[a] Laboratory of Chemistry and Materials Technology, Department of Agricultural Development, Agrifood and Natural Resources Management, National and Kapodistrian University of Athens, Psachna Campus, Evia 34400, Greece
[b] Nuclear Engineering Laboratory, Lithuanian Energy Institute, Breslaujos 3, LT-44403 Kaunas, Lithuania
[c] Heat Pipe and Thermal Management Research Group, College of Engineering, Design and Physical Sciences, Brunel University London, Uxbridge UB8 3PH, UK

ARTICLE INFO

Keywords:
Condensation
Monel 400
Corrosion behavior
Hydrofluoric-hydrochloric acids
Vapor-phase corrosion
Electrochemical analysis

ABSTRACT

This study assesses Monel 400's corrosion behavior in liquid and vapor phases in hydrofluoric (HF), hydrochloric (HCl), and mixed HF-HCl acid environments. Through mass loss testing and electrochemical measurements, the alloy's degradation was evaluated under varying acid concentrations, temperatures, gas atmospheres (N_2, O_2), and metal ion contaminants (Cu^{2+}, Fe^{3+}). Electrochemical measurements (ASTM G59/G102) and mass loss (ASTM G31/G1) were used for corrosion testing. The findings demonstrate that corrosion rates are considerably increased by vapor-phase exposure, especially in combined HF-HCl vapors (up to 0.8 mm·y^{-1}), because of combined fluoride and chloride chemical attack. Improved anodic dissolution and decreased passivation are confirmed by electrochemical data, particularly when oxidizing conditions (O_2) and Cu^{2+} and Fe^{3+} ions are present. Significant surface deterioration, dealloying, and the development of corrosion products rich in fluoride and chloride were discovered by SEM/EDS investigations. The addition of $CuCl_2$ and $FeCl_3$ changed the surface chemistry and increased localized corrosion. Similar degradation trends were shown by industrial validation in a condensing heat exchange unit employing Monel 400, where concentrated acidic condensates promoted rapid material loss and corrosion deposits consisting of chlorides. The findings emphasize the limitations of Monel 400 in HF-HCl systems, notably under vapor-phase and oxidizing conditions, and propose mitigation measures such as alternate Ni-Cr-Mo alloys, protective coatings, and oxygen exclusion to improve durability in harsh fluorinated environments.

1. Introduction

Monel 400 is a solid-solution Ni-Cu alloy that preserves its high strength and toughness over a wide temperature range and displays excellent corrosion resistance under diverse conditions. Such Ni-Cu alloys find applications in the aerospace, defense, marine, automotive, and power-generation systems [1–4]. Due to its superior seawater and chemical durability, Monel 400 is routinely applied for marine hardware and chemical-processing equipment, including process piping, boiler-feedwater heaters, and heat exchangers. It also displays exceptional resistance against hydrofluoric acid at all concentrations up to the boiling point and withstands sulfuric and hydrochloric acid solutions. However, its high density of 8.8 g·cm^{-3} and elevated melting point of 1300–1350 °C combined with a high heat resistance capacity, render Monel 400 poorly machinable under conventional cutting operations [5,6]. The nominal composition is listed in Table 1.

Corrosion is a significant issue across various industries due to its extensive economic, environmental, and safety implications. Corrosion is the "*physicochemical interaction between a metal and its environment that results in changes in the properties of the metal, and which may lead to significant impairment of the function of the metal, the environment, or the technical system, of which these form a part*" [7]. The direct costs of corrosion include expenses for inspection, maintenance, and repair of corroded equipment. Indirect costs, such as production downtime, loss of product, and decreased efficiency, can be several times higher than direct costs. These expenses can severely affect the profitability of

* Corresponding author.
E-mail address: vasta@uoa.gr (V. Stathopoulos).

https://doi.org/10.1016/j.tsep.2026.104642
Received 9 October 2025; Received in revised form 25 February 2026; Accepted 13 March 2026
Available online 20 March 2026

Table 1
Chemical Composition, %, of Monel 400.

Nickel (incl. Co)	Carbon	Manganese	Iron	Sulfur	Silicon	Copper
63.0 min	0.3 max	2.0 max	2.5 max	0.024 max	0.5 max	28.0–34.0

industrial operations. About 10 years ago, the National Association of Corrosion Engineers (NACE) published a study reporting that the estimated global cost of corrosion was approximately 3.4% of the global Gross Domestic Product [8] while in some studies as much as half of this cost refers to mitigation measures [9]. Measures against corrosion in the chemical industry are essential for ensuring safety, durability, cost efficiency, process integrity, regulatory compliance, and the ability to handle aggressive environments [10]. Material selection and protective coatings are two of the priority measures that can significantly reduce corrosion, leading to safer operations, longer equipment life, and lower maintenance costs [10,11].

The use of corrosion-resistant alloys such as Monel 400 is critical for maintaining the reliability and effectiveness of chemical processes and equipment. This includes the fluorochemical industry where corrosion issues with production process equipment require attention and innovative solutions, especially when ground-breaking technologies such as in the iWAYS project [12] are introduced in search of meeting the Sustainability Development Goals [13]. In the framework of the iWAYS project, three customized and integrated systems for a substantial reduction in thermal waste and freshwater consumption are fabricated, one of which is dedicated to an aluminum fluoride industry (Alufluor AB, Sweden). iWAYS systems will condense flue gases, while recovering heat that will be used to reduce primary energy consumption [14]. Implementation of this innovative technology imposes more rigorous performance criteria on structural alloys, as latent-heat recovery from flue gases exposes alloys to fluorine both in the gas and liquid state. Nevertheless, corrosion issues of production process equipment in the fluorochemical industry have been an open challenge for years. Although HF is classified as a weak acid in dilute solutions, it exhibits strong acidic behavior at higher concentrations as well as in aqueous solutions due to the inherent properties of HF (hydrogen bonding). Since water presence in the production process cannot be excluded, fluoride ions are released by HF [15]. In Ni-Cu alloys, a dense passive film is readily formed in the HF solution, and it mainly consists of Cu_2O and CuO. Therefore, Monel 400 is documented for its better corrosion resistance than Ni-Cr-Fe alloys and Ni-Cr-Mo alloys. Therefore, it is often used as engineering material for structural components in the fluorochemical industry [16,17].

Fluoride ions can diffuse due to their small size and charge and can penetrate the passive oxide layers that form on many metal surfaces. This process disrupts the protective barrier, leading to increased corrosion rates. Corrosion data of stainless steels with a high Ni-content and Ni based alloys in HF solutions were reviewed by Schillmoller, providing the framework for materials selection [18]. Corrosion data and degradation information of materials exposed to anhydrous hydrofluoric acid and HF mixtures with other acids and impurities were also reviewed by Jennings in 2001[19]. In 2007, the National Association of Corrosion Engineers (NACE) published NACE 5A171, setting the standards and criteria to address HF corrosion issues, in particular for storing and handling aqueous HF and anhydrous hydrofluoric acid. In the same year, the American Petroleum Institute (API) reported in API RP 751 on the possible corrosion failure of equipment during alkylation processes and provided corresponding recommendations and guidance. Up to 2021 the available literature reports a large amount of corrosion data of alloys in HF solutions but only limited data on the corrosion behavior and internal mechanisms are available. In 2021 Dai et al [15] published a review about the special attack characteristics of the fluoride ion, the corrosion mechanisms of nickel-based alloys in HF solutions or fluoride ion-containing environments, typical corrosion behaviors, and the influencing factors (e.g. alloying elements, environmental factors, and stress) on HF corrosion. Alterations in the passivation mechanism, the influence of HF attack modes and multiple damage mechanisms due to mechanical–chemical coupling were also identified.

Most metallic materials, including nickel-based alloys, likely undergo passivation when encountering acidic media such as HCl, H_2SO_4, and HNO_3 [20–25]. The passive film formed on the surface acts like a barrier to corrosive ions, but fluoride ions found in HF solutions disrupt the passivation layer, due to the active dissolution ability of fluoride ions. Lochel et al [26] pointed out that HF accelerated the transformation of oxides into fluorides on iron surfaces as a means of damaging the passive film. The active dissolution of fluoride damages the passive film either by rendering the compact passive film porous, or by forming semi-soluble fluorides through fluoridation.

Ni-based corrosion-resistant alloys typically exhibit superior corrosion resistance to localized corrosion compared to conventional austenitic stainless steels (e.g. 300-series) in chloride-containing aqueous environments, owing to their higher Ni and Mo contents. The corrosion mechanisms of Monel 400 and other Ni-based alloys (Ni–Cr–Mo and Ni–Cr–Fe) are similar to those of stainless steels, involving passivation weakening due to fluoride ion penetration [27–33]. The key difference is that in HF solutions, fluoridation and oxidation processes are inseparable for nickel-based alloys. [15] According to Yang et al [32,33] and Li et al [30], fluoride ions play a role in the passivation process of Ni–Cr–Mo alloys containing copper in HF solutions. Fluoride ions are incorporated into the passive film as copper fluorides alongside Ni, Cr, and Fe fluorides. Similarly, the presence of Ni, Cr, and Fe fluorides in the passive film indicates that it comprises not only of metallic oxides but also stable metal-fluorides. This suggests that fluoride ions are not always harmful in the corrosion of nickel-based alloys [30,31].

This synergistic mechanism of fluoridation and oxidation is also observed in Ni–Cr–Mo, Ni–Cr–Fe, and Ni–Cu alloys [16]. Various elements drive the passivation process, leading to different types of passive films that protect the surface from further corrosion. This element diversity results in the formation of unique protective films that enhance the corrosion resistance of each alloy by forming robust barriers against corrosive environments. For Ni–Cr–Mo alloys, the passive surface film primarily consists of Mo-rich substances, such as Mo oxides and hydrates [31]. In contrast, for Ni–Cr–Fe alloys, the passive film contains oxides, fluorides, and hydrates of Ni, Cr, and Fe, which exhibit higher thermal stability than Mo oxides and hydrates [16]. For Ni–Cu alloys, a passive film forms consisting of a Cu matrix, oxides, and fluorides, which show low degradation performance and minimal defects, effectively protecting against severe HF solution attacks [27,29,32,33]. Compared to the other two alloys, Ni–Cu alloys such as Monel 400 demonstrate the highest corrosion resistance due to the superior performance of their passive film. This film, composed of a copper matrix, oxides, and fluorides, effectively resists degradation and defects, providing robust protection against severe attacks from HF solutions [19,34–36]. This superiority is clearly illustrated in the most recent review published in 2021 [15] and by Dai et al [16].

However, different conclusions on the behavior of nickel alloys in wet hydrofluoric acid were reported in 2001 by Rebak et al [27]. The corrosion rate of a Ni-Cu and a Ni-Cr-Mo-Cu alloy increased with increasing acid concentration and temperature. The corrosion rate for the Ni-Cu alloy increased faster than that of the Ni-Cr-Mo-Cu alloy, especially in the vapor phase. Recently Guo et al [37] reported an unexpectedly high corrosion sensitivity of Monel 400 when exposed to HF vapor with a corrosion rate over 4.5 $mm \cdot y^{-1}$. Stress corrosion cracking (SCC) is also likelier to occur, raising concerns for the expected working lifespan of equipment manufactured with Monel 400 alloy [38]. Monel 400 also exhibits an anodic dissolution-corrosion mode, dominated by fluoridation, in an HF vapor environment. This leads to SCC under such conditions. Indeed, the fluoride ions play an important role in the

corrosion mechanism of Monel 400 in HF vapor. It is worth noting, though, that fluoride ions may exist in HF solutions without triggering the occurrence of SCC like in HF vapor [17,28,29,39,40]. This clearly indicates that the presence of fluoride ions is not only a necessary condition, but other parameters may also affect or even control the corrosion paths, such as the presence of oxygen in HF solutions, and the observed corrosion rate of Monel 400 was comparable to that in HF vapor [41]. Guo et al [37] reported that the corrosion rates increase from O_2-poor to O_2-saturated conditions for both vapor and liquid phases but a high O_2 content is not the primary factor causing more severe corrosion in the vapor phase. The formation of $NiF_2{\cdot}4H_2O$ instead of $CuF_2{\cdot}2H_2O$ is the main reason for the more severe corrosion as well as in the HF vapor phase, which is not caused by the high O_2 content. However, the conversion of Cu to Cu_2O is governed by oxygen presence. In other studies, the presence of green crystalline corrosion products consisting of $CuF_2{\cdot}2H_2O$ formed on Monel 400 after corrosion by HF vapor was also reported [27], markedly different from the chemical composition of the passive film generated in aqueous HF solutions. CuF_2 was linked to SCC and stress corrosion "poisoning" effects on Monel 400, causing the same failure even when introduced dissolved in HF solutions.

Graf et al [42] and Everhart [43] assumed that the generation of CuF_2 would lead to SCC of Monel 400 in contact with HF vapor, reporting that cracking occurred under stress in an HF solution containing CuF_2, the cracking mode being the same as in HF vapor. This also indicated that existence of CuF_2 had a stress corrosion "poisoning" effect on Monel 400 alloy, but the detailed poisoning mechanism of CuF_2 has not yet been revealed. Very recently, Dai et al. [44] reported that HF vapor on Monel 400 can lead to passivation failure by a high dissolution rate as oxygen not only promotes the oxidation of Cu, but also assists the active dissolution process of fluoride ions. In addition, CuF_2 is generated thinly, thus accelerating the denickelification of the matrix through the displacement reaction. Monel 400 corrosion found in the presence of Cu^{2+} ions is also of broad interest in other applications; for example, recent findings indicate that Monel 400 undergoes dealloying in the presence of Cu^{2+} ions. This becomes critical in nuclear steam generators where copper-enriched sludge piles create localized corrosion sites that compromise operation [45].

Although attempts have focused on revealing the corrosion mechanism of Monel 400 in HF vapor, the urgent need to investigate the contribution of the chemical environment composition of Monel 400 remains. Elucidation of the influence of the presence of co-existing strong acids such as hydrochloric acid that is readily available in industrial conditions, oxygen, or even other ions and by-products is also a pressing matter. Dry hydrogen chloride (HCl) is not corrosive to most metals but once dissolved in water hydrochloric acid is formed and is corrosive to many metals and alloys. Hydrochloric acid is an important mineral acid with many uses, including acid pickling of steel, acid treatment of oil wells, chemical cleaning and chemical processing. As a typical reducing acid, its cathodic reaction is hydrogen evolution upon contact with metals below hydrogen in the electromotive series. Dissolved oxygen or stronger oxidants promote the corrosion of many nonferrous metals above hydrogen as well. It should be noted that HCl acid concentrations less than 0.5% can be handled by Monel 400 and up to 20% at ambient temperature in reducing air-free systems. However, in practical conditions where oxygen and ions are dissolved as impurities, corrosion can be severe and the rate of attack is not always predictable [46,47].

While the behavior of metallic materials in corrossive HF solutions has been extensively investigated particularly for Ni-based alloys due to their paramount industrial significance [15–19,26–31] the majority of available studies focus on single-acid environments due to the inherent complicated nature of mixed acid solutions. HF is known to induce corrosion through fluoridation-driven deterioration of passive oxide films, ultimately leading to the formation of fluoride or oxyfluoride species [15,26,27]. In contrast, chloride-containing environments are typically associated with passive film degradation and localized corrosion phenomena [46,47]. Therefore, it is expected in mixed HF/Cl^- environments that these mechanisms co-exist and interact synergistically, resulting in conditions-specific corrosion behavior. Competitive adsorption of fluoride and chloride ions, formation of mixed halide complex ions, and case-sensitive corrosion product stability have been suggested to contribute to the overall behavior. Nevertheless, systematic experimental studies addressing specific HF-Cl^- mixtures remain limited, particularly for Ni-containing alloys under harsh conditions relevant to industrial exposure [15,27,37]. Our work aims to contribute to addressing this issue by examining corrosion behavior in combined environments under comparable conditions.

The current work investigates the corrosion behavior of Monel 400 in hydrofluoric (HF) and hydrochloric (HCl) acid environments through mass loss and electrochemical measurements. Specimens were subject to immersion and vapor-phase corrosion tests following ASTM G31 and ASTM G1 standards. Mass loss experiments were conducted in 40% w/v HF at 25 °C (liquid phase) and 60 °C (vapor phase), as well as in a mixed HF-HCl vapor environment for 108 h. Electrochemical measurements were performed in various HF and HCl concentrations. Additional tests under nitrogen and oxygen purging conditions assessed the influence of reducing and oxidizing environments on corrosion. Furthermore, the impact of Cu^{2+} and Fe^{3+} ions on corrosion mechanisms was evaluated using the corresponding chloride salts. Our findings provide insights into the degradation of Monel 400 in aggressive acid environments and the role of oxidizing species in accelerating corrosion. These measurements are correlated with an industrial case of the condensation unit installed at the Lithuanian Energy Institute (LEI) Nuclear Engineering Laboratory. Collectively, the results collected by such an upscaled unit provide an in-depth analysis of the implications under practical operational conditions where the specimens meet corrosion media in the vapor phase and subsequently in vapor and liquid phase when condensation occurs.

2. Materials and methods

2.1. Materials

The Monel 400 selected for this research was machined into cylindrical specimens of 1.38 in (~3.5 cm) diameter and a thickness of approximately 0.59 in (~1.5 cm). All sample surfaces and edges were first ground with a 240-grit finish followed by a final polish to a 600-grit finish and designated a sample number (Fig. 1). Before each test, samples were cleaned with methanol in an ultrasonic cleaner and then air-dried. Every sample was initially weighed and the surface area calculated for the mass loss experiments. An HF solution of 40% and HCl solution of 37% were purchased from Sigma Aldrich and also copper chloride dihydrate ($CuCl_2{\cdot}2H_2O$) (>99% purity) and iron chloride hexahydrate ($FeCl_3{\cdot}6H_2O$) (>97% purity, Sigma Aldrich). Finally, N_2 and O_2 gases purchased from Air Liquide with 99,999% purity were used

Fig. 1. Surface of Alloy 400 sample prior to experiments.

for electrochemical tests.

2.2. Mass loss test

Mass loss tests were performed under the techniques described in ASTM G31 "Standard Guide for Laboratory Immersion Corrosion Testing of Metals" and ASTM G1 "Standard Practice for Preparing, Cleaning, and Evaluating Corrosion Test Specimens". The alloy samples were tested in the liquid phase of 40% w/v HF at 25 °C in sealed propylene containers according to ASTM G31 "Standard Guide for Laboratory Immersion Corrosion Testing of Metals" and in the vapor phase at 60 °C in a closed plastic gasket containing vapors of 40% w/v HF (Fig. 2), see mass loss setup of (left) immersed samples at 25 °C in liquid 40% w/v HF, (center) exposed samples in 40% w/v HF vapor at 60 °C and (right) exposed samples in 40% w/v HF + 38% w/v HCl vapor at 60 °C. Furthermore, experiments were conducted in the vapor phase of both 40% w/v HF and 38% w/v HCl. Samples were exposed to the above conditions for a total of 108 h in order to estimate the corrosion rate. After exposure, samples were weighed to determine the mass loss according to ASTM G1 "Standard Practice for Preparing, Cleaning, and Evaluating Corrosion Test Specimens".

2.3. Electrochemical tests

Electrochemical tests were performed in a custom-made plexiglass cell of 50 mL volume capacity with a standard three-electrode setup (Fig. 3). The sample was attached to the working electrode exposing a surface area of 0.7854 cm^2, a saturated Ag/AgCl aqueous reference electrode (saturated Ag/AgCl) and a Pt-mesh counter electrode (99.999% purity). An Open-Circuit-Potential (OCP) test was performed for 30 min followed by Linear Polarization Plots (LP, Tafel Plot) with an AMETEK VersaSTAT 3 Potensiostat. LP measurements were conducted with a scan rate of 0.15 $mV{\cdot}s^{-1}$, at a potential window of –500 mV to 500 mV vs Ag/AgCl sat'd. Acid solutions used were 0.1 M HF, 0.1 M HCl, 1 M HF, 1 M HCl, and mixtures of 0.1 M HF with 10, 100, 1000 and 1800 ppm HCl. In addition, electrochemical experiments under flows of pure N_2 and pure O_2 (50 $mL{\cdot}min^{-1}$) were conducted to investigate the reducing and oxidizing conditions in the corrosion mechanism of Monel 400 in 0.1 M HF. The solution was continuously purged under bubbling conditions throughout the whole experiment. Experiments for the mixture solutions of 0.1 M HF with varying ppm HCl were deaerated by purging with N_2 and O_2 for 30 min prior to LP tests during the remainder of the test. A last set of experiments was conducted with 0.1 M HF

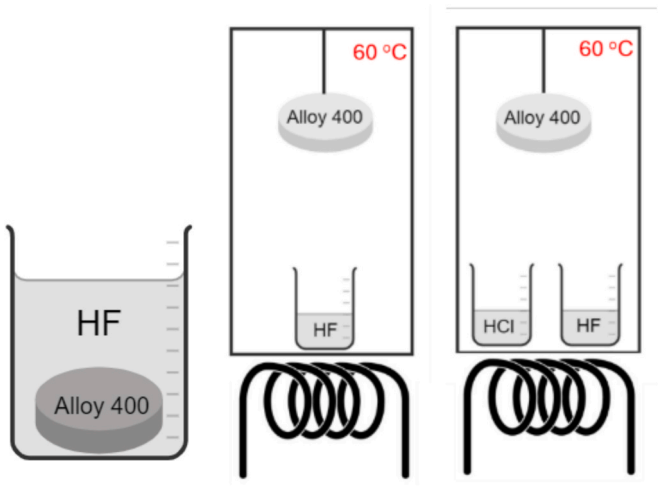

Fig. 2. Mass loss setup of (left) immersed samples at 25 °C in liquid 40% w/v HF, (center) exposed samples in 40% w/v HF vapor at 60 °C and (right) exposed samples in 40% w/v HF + 38% w/v HCl vapors at 60 °C.

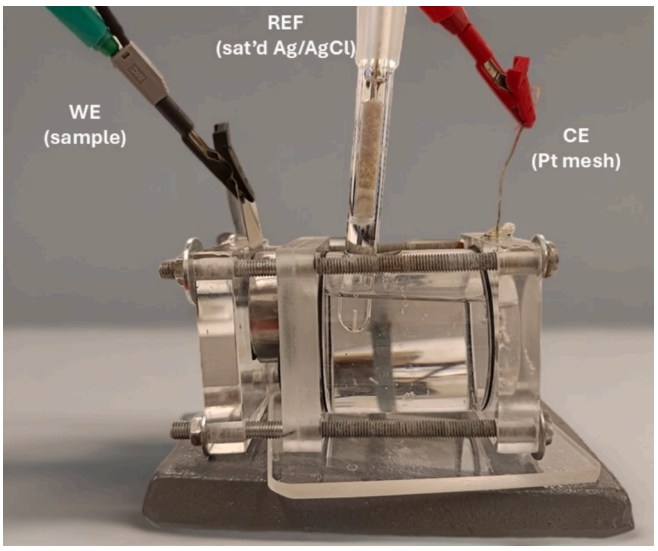

Fig. 3. Electrochemical Cell.

containing 700 ppm ferric and cupric ions in the form of chloride salts ($FeCl_3{\cdot}6H_2O$, $CuCl_2{\cdot}2H_2O$) in order to estimate the impact of Cu and Fe ions on corrosion mechanisms. All electrochemical tests and the respective environments are listed in Table 2.

2.4. Corrosion rate calculations

The corrosion rate was calculated from both mass loss and electrochemical experiments. In mass loss experiments the Corrosion Rate (mpy or $mm{\cdot}y^{-1}$) is calculated using the equation:

$$CR = \frac{ML \bullet K}{d \bullet A \bullet t} \quad (1)$$

where ML: mass loss in g, K: constant (equals to 87,600 for $mm{\cdot}y^{-1}$ and 3,450,000 for mpy), A: exposed area of Monel 400 in cm^2, d = 8.8 $g{\cdot}cm^{-3}$, t: time in h

In electrochemical experiments the calculation of corrosion potential (E_{corr}), corrosion current (I_{corr}) and Corrosion Rate (mpy, CR) was performed through the software of the potensiostat (Versa Studio) following the procedures described in ASTM G59-97 "Standard Test Method for Conducting Potentiodynamic Polarization Resistance Measurements". The corrosion rate is calculated through ASTM G102–23 "Standard Practice for Calculation of Corrosion Rates and Related Information from Electrochemical Measurements". More specifically, the

Table 2
Conditions of electrochemical experiments.

Solution in Electrochemical Cell	Purged Gas*
HF 1 M	Ambient
HCl 1 M	Ambient
HF + HCl 1 M	Ambient
HF 0.1 M	Ambient
HCl 0.1 M	Ambient
HF 0.1 M + HCl 0.1 M (1800 ppm)	Ambient
HF 0.1 M + 10 ppm HCl	Ambient
HF 0.1 M + 100 ppm HCl	Ambient
HF 0.1 M + 1000 ppm HCl	Ambient
HF 0.1 M	N_2
HF 0.1 M	O_2
HF 0.1 M + HCl 0.1 M (1800 ppm)	N_2
HF 0.1 M + HCl 0.1 M (1800 ppm)	O_2
HF 0.1 M + $CuCl_2{\cdot}2H_2O$ (700 ppm)	Ambient
HF 0.1 M + $FeCl_3{\cdot}6H_2O$ (700 ppm)	Ambient
HF 0.1 M + $CuCl_2{\cdot}2H_2O$ + FeCl2·.6H2O (both 700 ppm)	Ambient

* ambient = no gas flow.

CR is given by the equation below

$$CR(mpy) = \frac{0.13 \bullet I_{CORR} \bullet EW}{d} \quad (2)$$

where I_{corr}: corrosion current density in $\mu A \cdot cm^{-2}$, EW: equivalent weight of Monel 400 = 34.6 g, d = 8.8 $g \cdot cm^{-3}$. Corrosion rates are reported primarily in SI units ($mm \cdot y^{-1}$); equivalent values in mils per year (mpy), commonly used in industrial corrosion engineering practice, are provided using the conversion 1 mpy = 0.0254 $mm \cdot y^{-1}$.

2.5. Surface Characterization of materials

The surface morphology of selected electrochemically corroded samples was investigated by Scanning Electron Microscopy (SEM, Thermoscientific, Phenom XL), operating at 10–15 keV, equipped with an energy dispersive X-ray spectrometry (EDS) system. Specimens were placed on double-sided adhesive tape and sputtered with Pt in order to create a coating with a thickness of c.a. 10 nm.

2.6. Case study of an industrial condensation unit – experimental setup and operation

2.6.1. Experimental setup

An industrial economizer (Fig. 4), designed for operation with simulated gas (air, water vapor, and acid, was installed at the LEI Nuclear Engineering Laboratory. The condensation unit was designed by Brunel University, manufactured by Econotherm and used to perform experiments at LEI. The internal surfaces (top, bottom and walls) of the condensation unit were manufactured of Monel 400.

Dry air from the compressor was supplied to the air collector. The air flowed from the collector, through the airflow rate meters, to the air heaters (3 × 30 kW), where it was heated to the required temperature. After that, it flowed into the air and water vapor mixing chamber and, via a large-diameter pipe (Alloy 59, Ø271 × 4 mm), into the condensation unit, the external dimensions of which are 2370 × 500 × 1950 mm. It is composed of three sections of pipes. One section contains 40 pieces of pipe (a total of 120 pieces of pipe) arranged in 5 rows of 8 pipes (Fig. 5).

The pipes in each section of the condensation unit were placed in a staggered configuration with longitudinal pitch of 1.2 and transverse pitch of 1.5. The total length of one pipe is 1520 mm, with approximately 500 mm immersed in the cooling water, and the remaining length operating in the simulated gas area. The total outer surface area of all the pipes operating in the simulated gas area was ~ 12 m^2. During the experiments, only the pipes in section no. 1 were made of Monel 400 (Ø31.8 × 2.64 mm), while the pipes in sections no. 2 and no. 3 were made of 304 L.

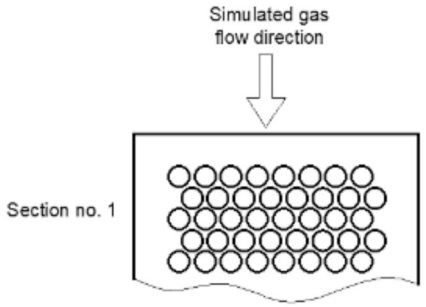

Fig. 5. Pipe specimens' arrangement in condensation unit (top view).

At the outflow of the condensation unit, the simulated gas was routed via the discharge pipe (pipe material stainless steel 304, Ø271 × 3 mm) to the exhaust stack and discharged into the atmosphere.

In order to have the necessary water vapor mass fraction (VMF) of the air being supplied to the condensation unit, steam from the steam generator (60 kW) was supplied to the mixing chamber. After the mixing chamber, at the beginning of the large-diameter pipe, an injector (type MH05) was mounted and connected to the acid supply (dosing) system (100 l tank with a peristaltic pump Dulcoflex DFXa). After the mixing chamber, the humidified air mixed with the injected acid. The acid evaporated, and the mixture of the humidified air and evaporated acid—i.e. simulated gas—was supplied to the condensation unit. To ensure that the injected acid had completely evaporated, a condensate collection tank was installed at the end of the large-diameter pipe just before the condensation unit. The absence of condensate in that tank during the experiments confirmed the complete evaporation of the injected acid. Additionally, the absence of droplets before the condensation unit was checked using water-sensitive paper, which was inserted at the end of the large-diameter pipe.

In the condensation unit, the evaporated acid and water vapor mixture condensed on the surfaces of pipes, and the condensate from each section flowed into separate condensate collection tanks.

Pipes installed in the condensation unit were cooled using water (cooling water in the condensation unit and simulated gas were circulating in the counter-current directions). The cooling water was supplied to the condensation unit by a pump, which delivered it through the water flow rate meter and water mixer. Before entering the condensation unit and after leaving it, the cooling water was mixed in the mixers to have a uniform temperature. Water supply via all three sections of the condensation unit was done in series. After leaving the condensation unit, hot cooling water was routed to the cooling tower, where it cooled down and was supplied again for the condensation unit cooling.

The entire test section and the chimney were thermally insulated.

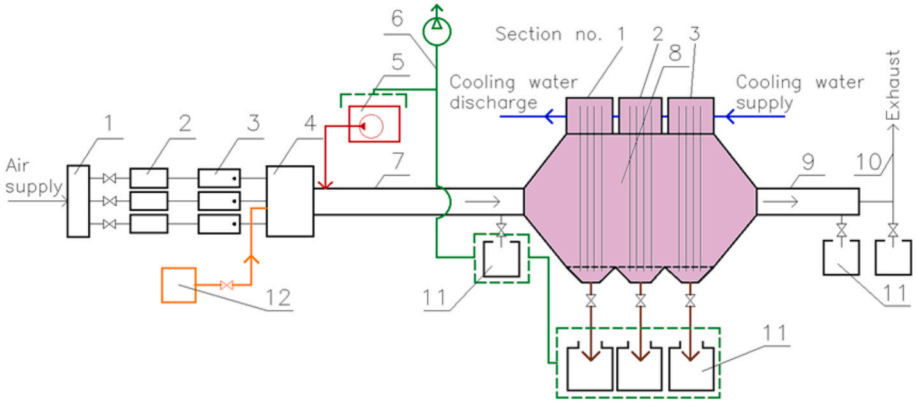

Fig. 4. Experimental setup: (1) air collector, (2) air flow rate meter, (3) air heater, (4) mixing chamber, (5) HCl acid dosing system, (6) harmful fumes extraction system, (7) large diameter pipe (8) heat exchanger, (9) discharge pipe, (10) exhaust stack, (11) condensate collection tank, (12) steam generator.

The air and steam mixing chamber, large-diameter pipe and condensation unit were insulated with two layers (50 mm each, total insulation thickness 100 mm) of Rockwool insulation. The discharge and exhaust pipes were insulated with 50 mm Rockwool insulation.

2.6.2. Operational conditions and experimental methodology

The air flow rate to the condensation unit was measured using three flow rate meters fitted at the air collector. Air heaters had installed thermocouples, which were used only to adjust the temperature of the simulated gas being supplied to the condensation unit. A vortex flow rate meter was mounted in the steam supply line. It measured the steam flow rate and temperature. Acid injection was realized using a peristaltic pump, allowing the necessary dosing flow rate of the acid to be set. The water vapor mass fraction in the air, along with the evaporated acid, was calculated based on the flow rates of supplied water vapor, acid, and air.

Average simulated gas temperatures were measured at the inlet and outlet of the condensation unit using two sets of three calibrated chromel-copel type thermocouples installed at each end of the condensation unit (i.e. three thermocouples at the inlet and three at the outlet). The average cooling water temperature at the inlet and outlet of the condensation unit was measured by three calibrated chromel-copel type thermocouples installed in each of the water mixers. The cooling water flow rate was measured by an electromagnetic water flow rate meter (Isomag), and the necessary flow rate was adjusted by the valve. During the experiments, all the thermocouple readings were collected using the automatic data acquisition system Keithley.

The acidic condensate before the heat exchanger (if any) and from its different sections was collected in separate condensation unit tanks of 10 l each. The amount (kg) of the collected condensate was evaluated based on the mass difference of the tank before the experiment and after it ended (weighing method). The condensate mass flow rate was determined based on the collected condensate mass per collection duration. For the determination of collection duration, a stopwatch was used. The condensate collection in the tanks during the experiments was started only after all experimental parameters had reached a steady-state condition. The collected condensate density was measured using a DMA 35 temperature and density meter. The concentration of HCl in the collected condensate was determined based on the condensate density and temperature.

The experiments were carried out at 330 kg/h simulated gas flow rate at the inlet to the condensation unit, inlet temperatures of 200 °C and 250 °C, inlet water-acid vapor mass fractions including evaporated acid 10% and 20% as well as a cooling water flow rate of 1320 kg/h with the inlet temperature of 23–25 °C. During the experiments, hydrochloric acid of 5% concentration was injected. The flow rate of the injected acid was 3.2 kg/h, which corresponded to ~ 220 ppm in the simulated gas flow. The high acid concentration (ppm) in the simulated gas enabled accelerated corrosion testing of the pipe material.

The analysis of solid sediments collected from internal surfaces of the condensation unit after the experiments was done using a scanning electron microscope (SEM). An energy dispersive spectrometer (EDS) was used for elemental mapping of the solid sediments.

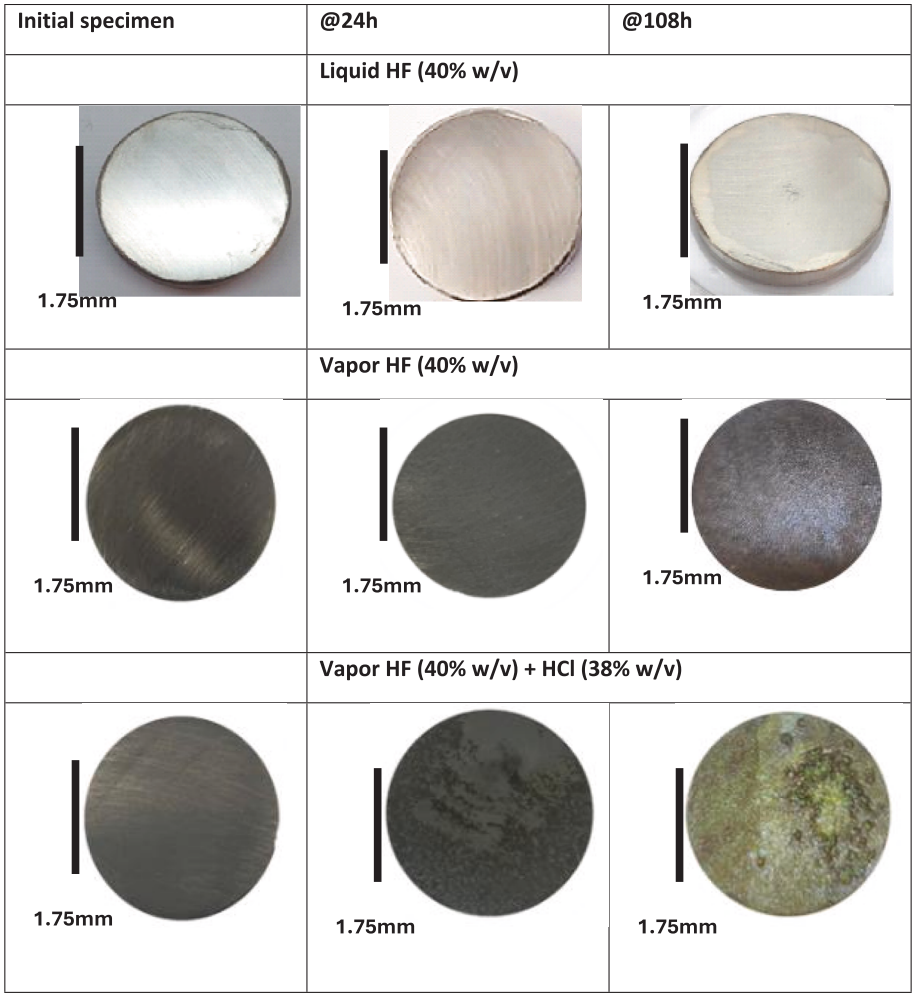

Fig. 6. Specimens of Monel 400 prior and after experiments on Mass Losses in different environments.

3. Results and discussion

3.1. Mass loss results

Results from mass loss experiments (Fig. 6) verified the issues described in the introduction. Aqueous HF solutions (wet conditions) showed minor visually-observed changes on the surface of Monel 400 after 108 h (4.5 days). The calculation of corrosion rate (CR, mm·y^{-1}) is shown in Fig. 6 and is equal to 0.04 mm·y^{-1}. This classifies the corrosion mechanism as mild and this is verified also by literature [48]. In the case of vapor 40% w/v HF the corrosion is enhanced ten-fold, leading to the conclusion that another mechanism is promoted in comparison with the liquid phase. Combining HF and HCl results in a 20-fold increased corrosion rate, leading to severe corrosion in both cases of vapor.

Visual changes of Monel 400 specimens under different corrosive environments reveal increasing degradation with increasing exposure time and environmental severity. The pristine specimen exhibits a smooth, polished surface. After 24 h in liquid HF (40% w/v), the specimen shows slight surface dulling, while at 108 h, it retains integrity with minimal surface changes, indicating mild corrosion. In vapor HF (40% w/v), the surface darkens significantly at 24 h, suggesting the formation of an initial corrosion layer, and after 108 h, the specimen appears rough with visible oxidation and discoloration, indicating a more aggressive attack. The most severe damage is observed in vapor HF (40% w/v) + HCl (38% w/v), where after 24 h, the surface already shows uneven corrosion patterns, and by 108 h, a heavily corroded and roughened morphology is evident, with greenish and oxidized regions, suggesting substantial material loss and chloride-induced attack. These results highlight that vapor-phase environments, especially with HCl, significantly accelerate corrosion compared to liquid-phase HF exposure.

The bar chart of Fig. 7 illustrates the corrosion rate (CR) of Monel 400 in different hydrofluoric acid (HF) environments, highlighting the influence of phase (liquid vs vapor) and temperature on corrosion severity. The x-axis represents the different test conditions, while the y-axis quantifies the corrosion rate in mm·y^{-1}. The data reveal a significant increase in corrosion rate as the exposure environment becomes more aggressive. In 40% w/v liquid HF at 25 °C, the corrosion rate is 0.04 mm·y^{-1}, indicating mild corrosion as denoted in green. This suggests that at lower temperatures and in the liquid phase, HF has a relatively limited corrosive effect on Monel 400. However, in 40% w/v HF vapor at 60 °C, the corrosion rate rises dramatically to 0.4 mm·y^{-1}, indicating a 10-fold increase in material degradation. This is due to the higher temperature and gaseous phase, which enhance the reactivity of HF, leading to accelerated corrosion in excellent agreement with recent findings [37]. The most severe corrosion occurs in a mixed vapor environment of 40% w/v HF and 38% w/v HCl at 60 °C, where the corrosion rate reaches 0.8 mm·y^{-1}. This highest rate of degradation suggests a strong synergistic effect between HF and HCl vapors, where the presence of HCl likely enhances metal dissolution and disrupts any protective film formation. Both temperature and phase change (liquid to vapor) significantly increase corrosion severity, with the most aggressive attack observed when HF and HCl vapors are combined. Considering recent reports by Guo et al [37] the reason can be the enhanced mass transfer to the alloy interface through a loose and porous corrosion product layer consisting of both fluoride and chloride deposits. Such a strong corrosion synergy when chlorides and fluorides coexist was reported for steel and Ti alloys by [49]. An interesting fact is that under condensation conditions the vapor phase corrosion deposits will be readily encountering the condensate. Thus, dissolution phenomena will take place enhancing further the dissociation of the corrosion product layer. An HCl solution will readily dissolve any copper or cuprous oxide formed on the surface, furthermore, for the case of chlorides or fluorides.

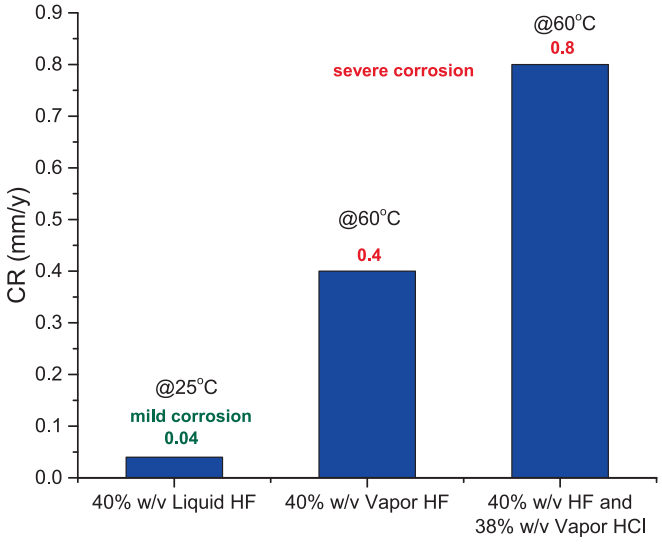

Fig. 7. Corrosion rate calculations from mass-loss experiments. Corrosion severity categories ("mild", "medium", "severe") are empirically defined in this work for comparative purposes (mm·y^{-1}: 0.00–0.05, 0.05–0.15, ≥ 0.15). These thresholds do not correspond to standardized corrosivity categories (e.g., ISO 9223), which are defined for atmospheric exposure of benchmark metals.

3.2. Electrochemical results

The results from electrochemical tests are indicative of the concentration effect of either HF or HCl acids. Tafel plots are presented in Fig. 8 and Fig. 9. Fig. 8 depicts the effect of the concentration of 0.1 M and 1 M on the corrosion behavior of Monel 400 in HF, HCl and combined solutions. The corrosion is enhanced by increasing the concentration while in 1 M HCl the indicative two peaks in the potential axis signify a more complex mechanism of the corrosion from HCl. The double peak profile indicates a multi-step corrosion mechanism, based on the distinct behavior of Ni and Cu constituents of the alloy; similar dual-peak behavior has also been reported for pure Cu in chloride media and for Cu-Ni alloys, linked to CuCl/Cu_2O formation and further oxidation to CuO/$Cu(OH)_2$ or to Ni-oxide growth [50,51]. Thus, the overall corrosion most probably involves the contribution of two different species. From Table 2 in 1 M concentrations, the corrosion rate reached 0.051 mm·y^{-1} for the combined HF + HCl solution which exceeds the sole effects of 1 M HF (CR = 0.031 mm·y^{-1}) and 1 M HCl (CR = 0.018 mm·y^{-1}). This indicates a synergistic corrosive mechanism of HF with HCl.

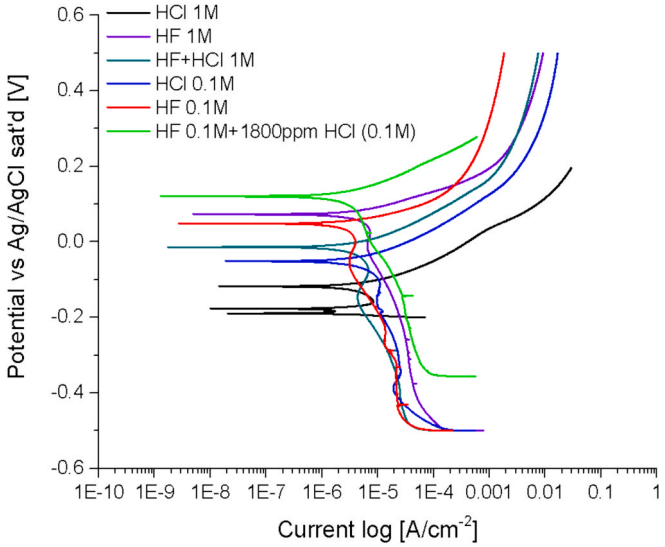

Fig. 8. Tafel Plots in 0.1 M and 1 M of HF and HCl.

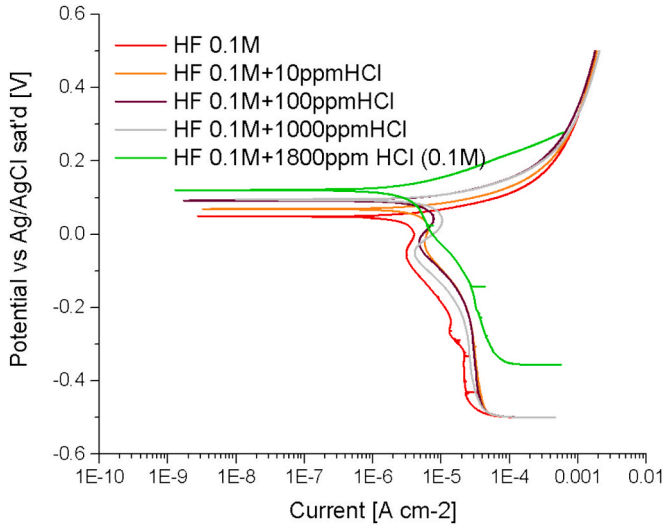

Fig. 9. Tafel Plots of gradual addition of HCl to 0.1 M HF.

In Fig. 9, the potentiodynamic polarization curves presented in the diagram illustrate the corrosion behavior of Monel 400 in various acidic environments, including hydrochloric acid (HCl), hydrofluoric acid (HF), and their mixtures. The differences in corrosion potential (E_{corr}) highlight the varying degrees of corrosive attack under these conditions. Comparing the individual acids, it is evident that 1 M HCl exhibits a relatively more negative corrosion potential than HF solutions, while also maintaining a lower corrosion current density. This suggests that Monel 400 experiences slower corrosion kinetics in HCl alone compared to HF. However, the presence of HF, either alone or in combination with HCl, significantly increases the corrosion current density, indicating a more aggressive dissolution of the alloy. Notably, the mixture of HF and HCl (1 M each) results in even higher current densities, confirming a synergistic effect where the combination of these acids accelerates the corrosion rate.

The higher current densities in the above mixture are attributed to the increased concentration of reactive species and higher overall acidity. Specifically, when both HF and HCl are present at higher molarities, the solution provides abundant fluoride (F^-) and chloride (Cl^-) ions, greatly enhancing ionic conductivity and facilitating efficient charge transfer during electrochemical reactions. The case of the lower potential of the 1 M mixture can be explained primarily by thermodynamic and kinetic considerations. When both acids are present at higher concentrations, the significantly increased availability of protons (H^+) reduces the activation barrier for cathodic reactions (such as hydrogen evolution). This lowers the activation polarization, allowing the reaction to occur at a lower (more negative) potential.

Furthermore, the elevated concentration of ions (particularly chloride and fluoride ions) enhances solution conductivity and electrolyte aggressiveness, facilitating faster reaction kinetics and further reducing overall polarization resistance. As a result, the system reaches higher current densities at lower applied potentials, shifting the electrochemical reactions toward more negative potentials. In contrast, the diluted solution (1800 ppm HCl in 0.1 M HF) experiences higher polarization resistance due to limited ionic conductivity and lower proton concentration. Consequently, reactions occur at relatively higher potentials and lower current densities [52–54].From an electrochemical point of view, the increased anodic dissolution is likely due to the role of chloride ions in disrupting passive films and facilitating localized attack, making the alloy more susceptible to degradation. In more dilute conditions, 0.1 M HF exhibits the lowest current density among the HF-containing solutions, indicating a reduced corrosion rate at lower HF concentrations. However, the introduction of HCl, even at low concentrations such as 1800 ppm, leads to a noticeable increase in the anodic current. This suggests that even small amounts of chloride ions in HF solutions significantly enhance corrosion activity.

The potentiodynamic polarization curves in Fig. 9 illustrate the influence of increasing HCl concentrations on the corrosion behavior of Monel 400 in 0.1 M HF. The curves exhibit a shift in both the corrosion potential (E_{corr}) and corrosion current density (I_{corr}) with increasing HCl concentration, indicating changes in the electrochemical activity. As the concentration of HCl increases from 10 ppm to 1800 ppm, a gradual increase in I_{corr} is observed, suggesting an acceleration in the corrosion rate. This aligns with the previously presented table, where higher HCl concentrations lead to increased material degradation. The anodic branch of the polarization curves demonstrates that passivation is not pronounced, meaning that Monel 400 does not form a stable protective layer in these conditions and the presence of chloride ions enhances localized attack [55,56]. Moreover, the cathodic region exhibits an increase in current density with rising HCl content, suggesting a more efficient cathodic reaction, possibly due to the depolarizing effect of chloride ions. The trend in the curves confirms that the combined presence of HF and HCl significantly impacts the corrosion kinetics, with higher chloride concentrations leading to more aggressive corrosion of Monel 400.

In Fig. 10, the red trace (0.1 M HF) exhibits an active dissolution region, suggesting continuous metal dissolution without a significant passivation effect. The green curve (0.1 M HF + O_2) shows an increased anodic current at higher potentials, indicating that oxygen enhances corrosion, likely due to its role as an oxidizing agent that accelerates the dissolution of the alloy. This suggests the formation of soluble corrosion products rather than a protective passive layer. In contrast, the blue trace (0.1 M HF + N_2) demonstrates a lower anodic current, implying that nitrogen provides a more inert environment, reducing oxidation and corrosion rates. This behavior indicates that oxygen plays a crucial role in promoting corrosion in HF, whereas the absence of oxygen in the nitrogen-purged solution mitigates the electrochemical reaction, leading to lower corrosion rates. Overall, the polarization curves reveal that Monel 400 experiences more aggressive corrosion in the presence of oxygen, while nitrogen-saturated conditions help suppress corrosion activity.

Comparatively, in Fig. 11, the 0.1 M HF shows the lowest corrosion current density. The passive region appears relatively stable before a sharp increase in current, indicating a breakdown of passivity and onset of active corrosion. The potential shifts negatively in the cathodic region, suggesting strong dissolution in fluoride-containing environments. In the case of 0.1 M HF + $CuCl_2$ a shift of the potential toward higher current densities indicates an increase in corrosion rate due to the

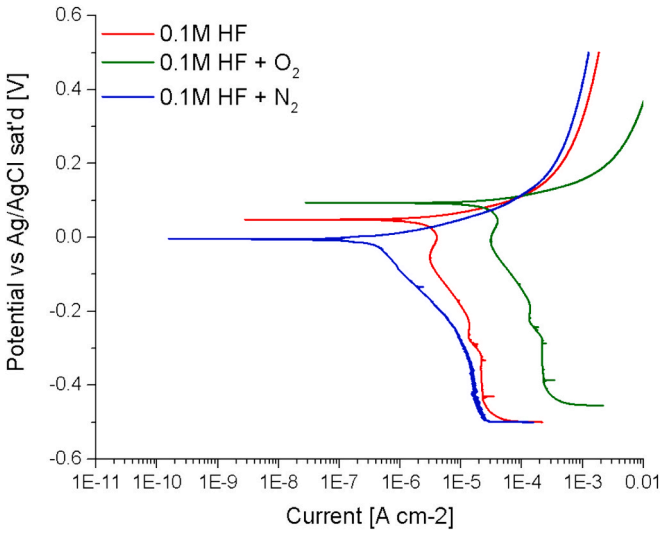

Fig. 10. Tafel Plots of 0.1 M HF under N_2 and O_2 gas streams.

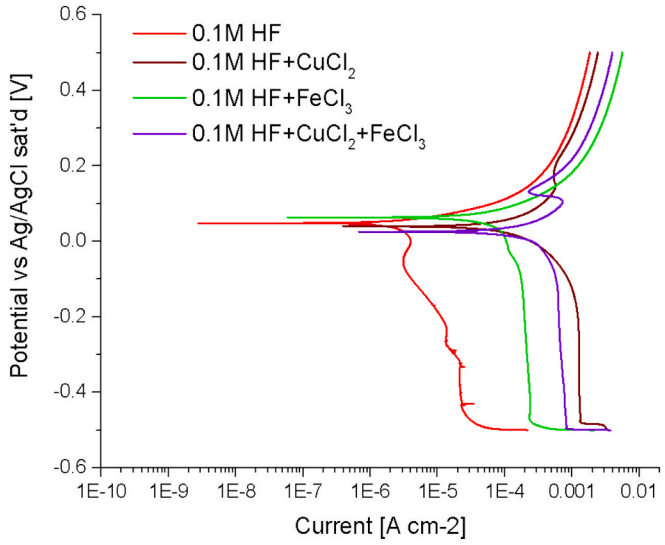

Fig. 11. Tafel Plots of 0.1 M HF with 700 ppm of Cu and Fe chloride salts.

presence of Cu^{2+} ions. These copper ions can participate in redox reactions, facilitating the cathodic process and accelerating metal dissolution. Further, in solutions of 0.1 M HF + $FeCl_3$ an evidently higher corrosion current compared to the $CuCl_2$-containing solution is observed. Ferric chloride is a strong oxidizing agent that enhances metal dissolution by promoting depassivation, and a pronounced increase in anodic current suggests aggressive localized corrosion or pitting. Finally, the highest corrosion current density among all compositions is observed in the case of 0.1 M HF + $CuCl_2$ + $FeCl_3$. The combination of Cu^{2+} and Fe^{3+} ions contribute to synergistic effects, intensifying both anodic dissolution and cathodic reduction. The earlier breakdown of passivity suggests severe corrosion behavior, likely due to enhanced pitting and localized attack. In order to quantify the above indications Table 3 provides the calculated results on corrosion rates of the electrochemical tests based on Eq.2.

The values of corrosion rates (CR), as calculated from electrochemical results, are depicted in Fig. 12 for all the samples tested. The horizontal axis represents the number assigned to each experiment (according to Table 2) and the vertical axis represents the corrosion values of each experiment in mpy.

Table 3
Tafel plot parameters' calculations and corrosion rates.

A/A	Solution	E_{CORR} [mV]	I_{CORR} [$\mu A \cdot cm^{-2}$]	CR ($mm \cdot y^{-1}$)	CR (mpy)
1	HF 1 M	77.87	2.46	0.031	1.26
2	HCl 1 M	117.34	1.37	0.018	0.70
3	HF + HCl 1 M	102.81	3.95	0.051	2.02
4	HCl 0.1 M	60.77	1.09	0.014	0.56
5	HF 0.1 M	50.95	0.73	0.009	0.37
6	HF 0.1 M (N_2)	4.61	0.19	0.003	0.09
7	HF 0.1 M (O_2)	95.08	2.34	0.024	0.94
8	HF 0.1 M + 10 ppm HCl	68.25	0.79	0.010	0.40
9	HF 0.1 M + 100 ppm HCl	89.98	0.89	0.011	0.45
10	HF 0.1 M + 1000 ppm HCl	94.74	1.06	0.013	0.54
11	HF 0.1 M + 1800 ppm HCl	122.58	1.16	0.015	0.59
12	HF 0.1 M + $CuCl_2 \cdot 2H_2O$ (700 ppm)	40.23	4.33	0.044	1.73
13	HF 0.1 M + $FeCl_3 \cdot 6H_2O$ (700 ppm)	62.56	7.89	0.079	3.17
14	HF 0.1 M + $CuCl_2 \cdot 2H_2O$ + $FeCl_3 \cdot 6H_2O$ (both 700 ppm)	25.69	8.58	0.087	3.44

The electrochemical results demonstrate the influence of acid concentration, gas purging, and metal ion additives on the corrosion behavior of Monel 400. Corrosion rates (CR) in pure acids indicate that 1 M HF (1.26 mpy) is more aggressive than 1 M HCl (0.70 mpy), while their combination further increases the corrosion rate (2.02 mpy). Diluted solutions (0.1 M) exhibit lower corrosion rates, with HF (0.37 mpy) and HCl (0.56 mpy). The introduction of N_2 significantly reduces corrosion in 0.1 M HF (0.09 mpy), whereas O_2 increases it (0.94 mpy), highlighting the role of oxidizing conditions. The addition of HCl in ppm levels gradually raises the corrosion rate, reaching 0.59 mpy at 1800 ppm HCl. Notably, the presence of Cu^{2+} ions (1.73 mpy) and Fe^{3+} ions (3.17 mpy) drastically accelerate corrosion, with their combination further increasing the corrosion rate to 3.44 mpy.

The SEM images provided (Fig. 13) illustrate the surface morphology of Monel 400 under various chemical environments, highlighting the effects of different corrosive media. In the first row, SEM images demonstrate the alloy's response to hydrofluoric acid (HF) under different ambient conditions. Monel 400 in HF presents a relatively smooth surface with minor pitting, as expected due to only mild corrosion. The second image (HF under N_2) exhibits a clean surface with few corrosion pits, suggesting that under nitrogen no surface deposition or changes are observed, in agreement with electrochemical measurements. When the corrosion medium is O_2-rich, the surface becomes slightly rougher compared to the N_2 environment with some visible depositions. In the second-row different acid exposures are recorded with small changes for HF and HCl. Both conditions have a moderate effect. However, under an HF + HCl combination significant corrosion deposits are observed, resulting in a rough surface with localized attack points. The combined effect of HF and HCl seems to cause accelerated corrosion. In the case of added ions as possible accelerators, the images highlight what can be calculated from the Tafel plots. In the presence of a different type of $CuCl_2$ crystalline formations are visible. When tested under $FeCl_3$, surface deposits of a different microstructure are present. The last image from the HF + $FeCl_3$ + $CuCl_2$ system is the most extreme case of surface formation, with an interconnected network of corroded regions forming a complex, porous morphology, indicating that the combined effect of $FeCl_3$ and $CuCl_2$ results in the most aggressive attack, in perfect agreement to the calculated corrosion rate.

The layered deposits of corrosion products can be beneficial for the protection of the underlying alloy, as (depending on their compactness) they may act as a physical barrier inhibiting further diffusion of corrosive ions from the bulk solution. Based on EDX analysis (Fig. 14), interesting variations are observed among samples due to the different solution chemistry during testing. When testing in the presence of $CuCl_2$, $FeCl_3$ or both, significant changes in the surface composition of the samples are found.

In the sample exposed to HF + $CuCl_2$, oxygen reaches 15.6 wt% and chlorine 14.8 wt%. This indicates substantial formation of oxides, chlorides and no fluorides. Considering that the surface composition is greatly enriched in Cu (64.1 wt%) and depleted in Ni (5.1 wt%) likely forming a rather inhomogeneous layer of Cu_2O and/or $CuCl_2$ as well as smaller amounts of NiO and/or $NiCl_2$, the corrosion rate is 4.7 times higher compared to HF alone.

When the liquid that encounters Monel 400 contains HF and $FeCl_3$ the corrosion rate becomes 8.6 times higher compared to HF alone, and the surface chemistry of the corrosion products is very different than when only copper ions are present. A layer of oxides (2.4 wt% O) seems to form along with a very small percentage of chlorides (0.3 wt% Cl) and no fluorides. Considering the high corrosion rate and the fact that the Ni/Cu ratio is merely altered, a rather thin formation of deposits or the formation of soluble corrosion products may be expected, leaving behind a porous deposition prone to mass transfer.

A further increase in the corrosion rate up to 9.3 times higher

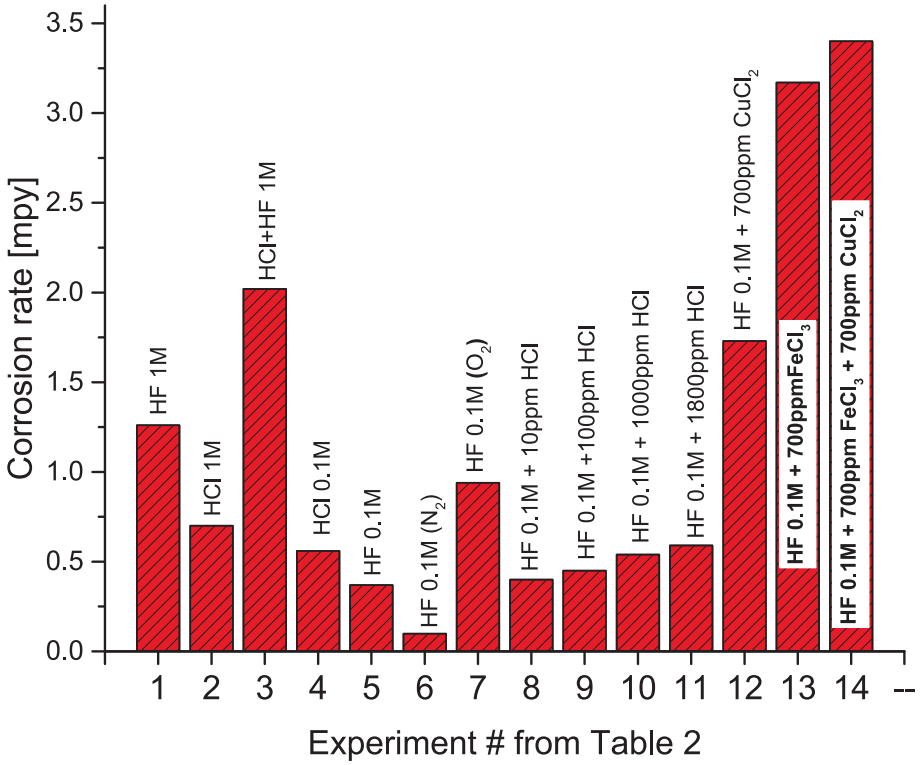

Fig. 12. Corrosion rates of all electrochemically tested specimens.

compared to HF alone, is found for Monel 400 in an HF + $FeCl_3$ + $CuCl_2$ environment. The surface composition is greatly enriched in Cu (66.9 wt %) and severely depleted in Ni (7.3 wt%) and the remaining elements i. e. Fe, Mn. Chlorine reach 25.6 wt%, indicating a strong likelihood of forming copper chloride ($CuCl_2$), iron chloride and possibly nickel chloride ($NiCl_2$) but no oxides. This indicates that the coexistence of Cu^{2+} and Fe^{3+} facilitates dealloying and the overall fast transition from Cu to Cu_2O and finally Cu^{2+} thus forming chlorides. The depletion of oxides in favor of chlorides indicates a physical barrier of poor density allowing the diffusion of corrosive ions from solution to the substrate. This agrees with previous findings, for example, Guo et al [37].

The above findings are in line with the SEM observations (Fig. 13) with significantly different top view formations among the samples.

A very different corrosion path seems to be followed when only HF is present, generating surface fluorides (2.8 wt% F), but no oxides were identified by SEM-EDX, keeping a stable ratio among the main alloying elements Ni/Cu. The absence of an oxide layer by HF corrosion in liquid conditions may be attributed to the detection limitations of the EDX analysis.

When only HCl acid is present, corrosion products consist of chlorides only (4.23 wt% Cl) without any oxides identified by EDX while the Ni/Cu ratio is slightly depleted in Cu. Moderate chloride presence is also observed in HF + HCl (3.6 wt% Cl) while fluorides are also abundant (3.3 wt% F). In the latter case, surface composition is greatly affected, being significantly depleted in Ni (52.3 wt%) and enriched in ratio for Cu (29.9 wt%). The above indicate a combined corrosion effect when both HF and HCl are present.

Surface fluoride formation is noticeable in conditions with significant fluorine content, particularly in HF + HCl (3.3 wt%) and HF alone (2.8 wt%). Considering the slightly depleted Ni/Cu ratio the potential formation of nickel fluoride (NiF_2) and copper fluoride (CuF_2) is expected.

In the case of HCl corrosion a significant amount of chlorides is formed (4.2 wt% Cl) while the Ni/Cu ratio becomes 2.0, indicating a lower Cu surface presence. Thus, the formation of soluble green deposits of $CuCl_2{\cdot}xH_2O$ and $NiCl_2{\cdot}xH_2O$ is expected.

The correlation between mass loss and electrochemical results for Monel 400 in different environments highlights the increasing severity of corrosion due to phase transition (liquid to vapor), acid concentration, and chloride-containing environments. From the mass loss experiments, the corrosion rate in 40% w/v liquid HF at 25 °C is 0.04 mm/y, classifying it as mild corrosion. This aligns well with electrochemical results, where 0.1 M HF (representing diluted HF conditions) exhibits a low corrosion current density and a corrosion rate (CR) of 0.009 mm/y. However, in vapor-phase HF at 60 °C, the mass loss corrosion rate increases to 0.4 mm/y, a tenfold rise compared to liquid HF, indicating that the corrosion mechanism in vapor is different, significantly enhancing the effect. Electrochemical data support this observation, as high HF concentrations (1 M) lead to an increased corrosion rate of 0.031 $mm{\cdot}y^{-1}$, demonstrating that acidity and fluoride ion activity enhance metal dissolution. The most severe corrosion is observed in HF + HCl vapor (40% HF, 38% HCl), where the mass loss corrosion rate reaches 0.8 $mm{\cdot}y^{-1}$, a 20-fold increase compared to aqueous HF. Electrochemical measurements confirm this trend, as the synergistic effect of HF and HCl (1 M) results in the highest electrochemical corrosion rate of 0.051 $mm{\cdot}y^{-1}$, surpassing the individual contributions of 1 M HF (0.031 $mm{\cdot}y^{-1}$) and 1 M HCl (0.018 $mm{\cdot}y^{-1}$).

The synergistic effect of HF and HCl is evident in both electrochemical and mass loss results, where the combination of these acids enhances corrosion significantly. Tafel plots (Figs. 7 and 8) reveal higher corrosion current densities in mixed HF + HCl solutions, while mass loss specimens exposed to HF + HCl vapor show extreme surface degradation, with roughened, discoloured, and significantly deteriorated surfaces. This suggests that chloride ions enhance metal dissolution by disrupting passive film formation and increasing localized attack. Additionally, oxidizing and inert gas conditions influence corrosion behaviour. Electrochemical polarization results (Fig. 9) indicate that oxygen enhances corrosion, whereas nitrogen suppresses it, confirming that oxidation-driven mechanisms accelerate metal dissolution. Mass loss images reflect this trend, where HF vapor-exposed specimens show

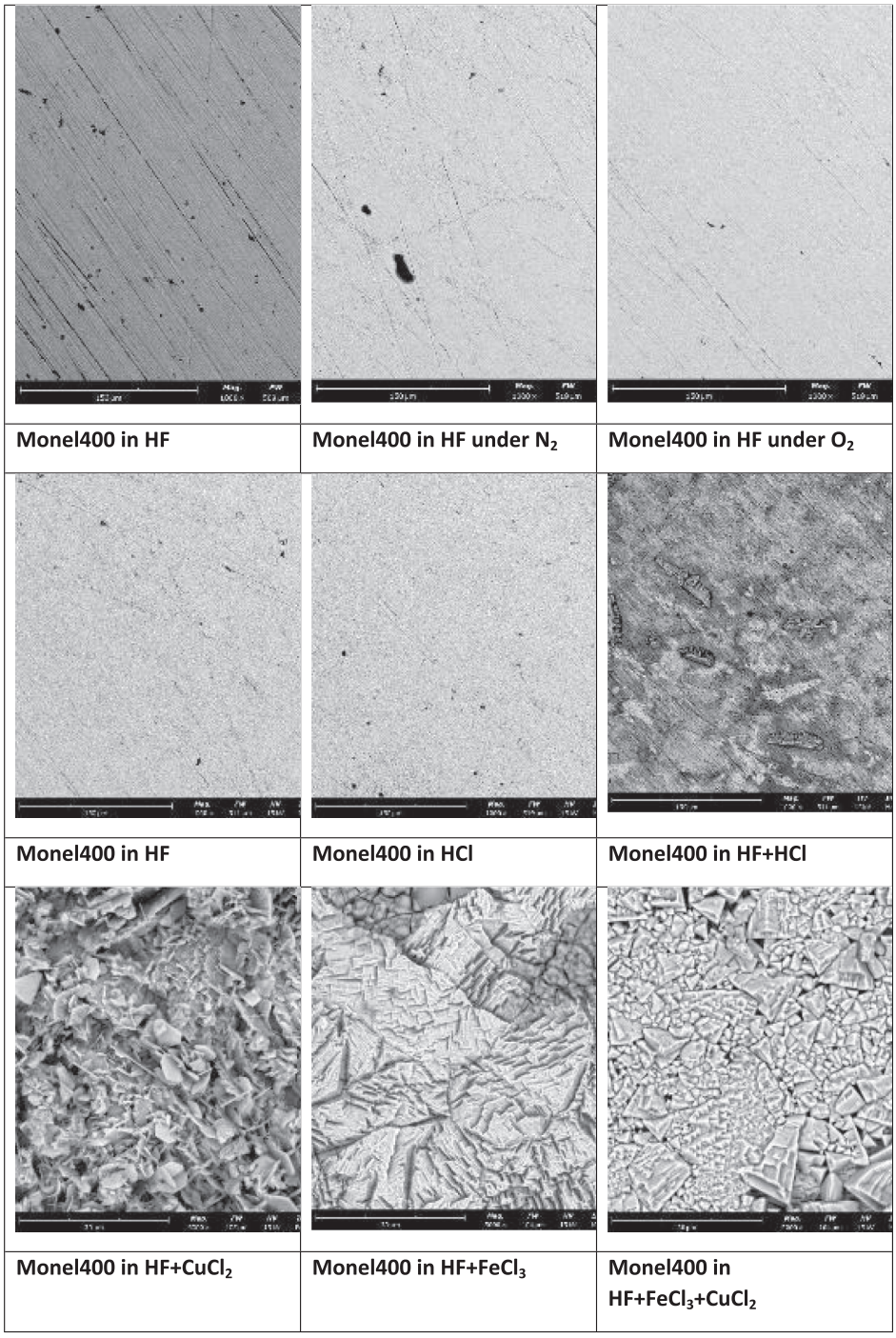

Fig. 13. Morphology of specimens after electrochemical tests.

more pronounced oxidation and corrosion compared to those in aqueous HF.

The influence of metal chlorides, specifically $CuCl_2$ and $FeCl_3$, also plays a critical role in corrosion acceleration. Electrochemical results (Fig. 10) demonstrate that Fe^{3+} induces the highest corrosion rate, followed by Cu^{2+}, with the combination of both leading to the most aggressive attack (CR = 0.087 mm·y^{-1}). This is in agreement with mass loss and SEM/EDX analyses, where specimens exposed to HF + $CuCl_2$ and HF + $FeCl_3$ exhibit extensive pitting, rough textures, and severe localized attack, suggesting that these chloride ions facilitate active dissolution and depassivation.

Overall, clear patterns emerge from both methodologies. Aqueous HF exposure results in minimal corrosion, as evidenced by both low mass loss rates and electrochemical CR values. In contrast, vapor-phase HF significantly enhances corrosion, likely due to a higher reactivity and the inability to form a protective layer. This may be also associated with differences in reaction kinetics and surface-film formation under non-immersed conditions. The most aggressive attack occurs in HF + HCl vapor, where chloride ions synergistically amplify metal dissolution. Furthermore, oxygen-rich conditions accelerate corrosion, while nitrogen-purged environments show reduced electrochemical activity and corrosion rates. Finally, chloride-containing environments ($CuCl_2$, $FeCl_3$) further amplify corrosion, promoting localized attack, pitting, and dealloying.

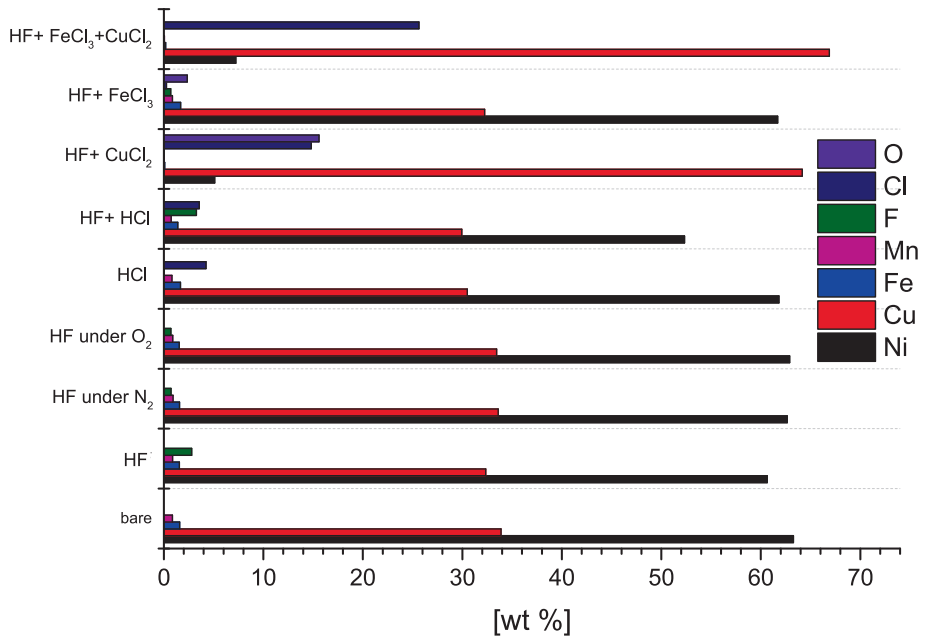

Fig. 14. EDX surface analysis on specimens after electrochemical tests on Alloy 400 with specific conditions.

Both mass loss and electrochemical results confirm that temperature, phase (liquid vs. vapor), acid concentration, and chloride ions significantly impact corrosion severity. The correlation between higher corrosion current densities, increased mass loss rates, and surface degradation across different methods provides a consistent understanding of Monel 400 degradation mechanisms in HF, HCl, and mixed environments.

The detrimental effect of the presence of oxygen in the corrosion of alloys is well-documented in the literature. Both early and contemporary studies concur that even a trace oxygen presence accelerates Monel 400 attack in HF-containing systems. Data in Nickel Institute Corrosion Engineering Bulletin [18] show that the absence of O_2 suppresses corrosion from ~ 30–40 mm·y^{-1} to ~ 0.1–0.2 mm·y^{-1}, whereas introducing as little as 500 ppm O_2 doubles the rate. The corrosion rate of Monel 400 in 49 wt% HF was found to increase ~ 6-fold when the atmosphere was switched from deaerated to air [28]. Furthermore, Dai et al [44] show that oxygenated HF vapor disrupts and removes the protective CuF_2/NiF_2 scale and promotes rapid denickelification, while Guo et al. [37] demonstrated that oxide-rich deposits that formed only under O_2-presence acted as catalytic wicks that amplify subsequent fluorination and metal loss.

3.3. Condensation unit results

For a proper analysis of the condensation process, it is important to know the dew point temperatures of the components. The HCl acid dew point temperature was determined using the graph presented in Fig. 15. The graph indicates the HCl dew point temperature at certain HCl concentrations in various water vapor volume fractions [57]. Water vapor mass fractions were in the range of 10% to 20%, which corresponds to 15% to almost 25% of volume fractions. Unfortunately, in [57], there are no dew point temperature curves for 20–25% water vapor volume fraction; therefore, this curve was obtained by extrapolation. According to Fig. 15, it is evident that the acid dew point increases with the increase in the acid concentration as well as with the increase in the water vapor fraction.

During the experiments, the injected HCl acid concentration was 220 ppm. Therefore, the HCl acid dew point was in the range between 57 °C and about 68 °C. In the case of pure water vapor, its dew point temperatures at mass fractions of 10% and 20% are ~ 53 °C and ~ 65 °C,

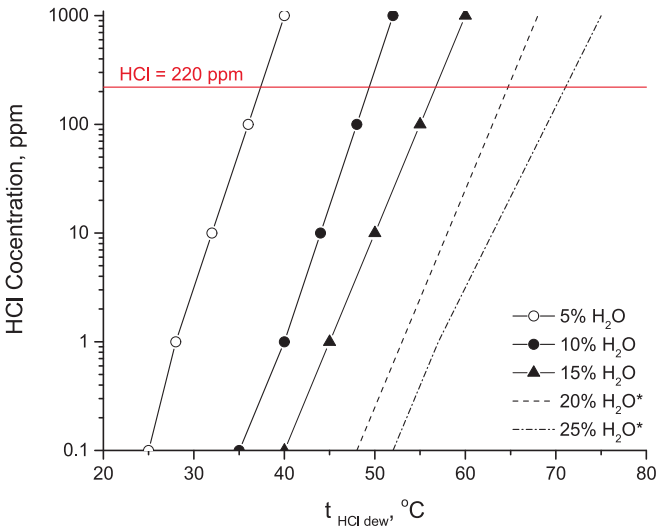

Fig. 15. HCl acid dew point temperature dependency on acid concentration in the gas with a certain water vapor volume fraction [57].

respectively. Thus, the acid dew point temperatures are higher than water vapor dew point temperatures, and therefore the acids begin to condense earlier in comparison with the pure water vapor. Typical distribution of the condensate flux in different sections of the condensation unit during the experiments is shown in Fig. 16. In the case of the simulated gas inlet temperature of 200 °C (Fig. 16a) and VWM = 10%, the smallest condensate flux of 0.25 kg/(m^2·h) was obtained from section no. 1 containing Monel 400 pipes. In section no. 2, the condensate flux obtained was about six times larger compared to that in section no. 1. In section no. 3, the condensate flux was almost the same as in section no. 2. An increase in the VMF to 20% increased the condensate flux (Fig. 16a) by almost 4 times in section no. 1, and in sections no. 3 and 4, the increase was approximately two times in comparison to that at VWF = 10%.

A higher simulated gas inlet temperature of 250 °C (Fig. 16b) resulted in an evident decrease in the condensate flux, mainly in section no. 1 (cf. Fig. 16a and b). In sections no. 2 and 3, there was only a slight

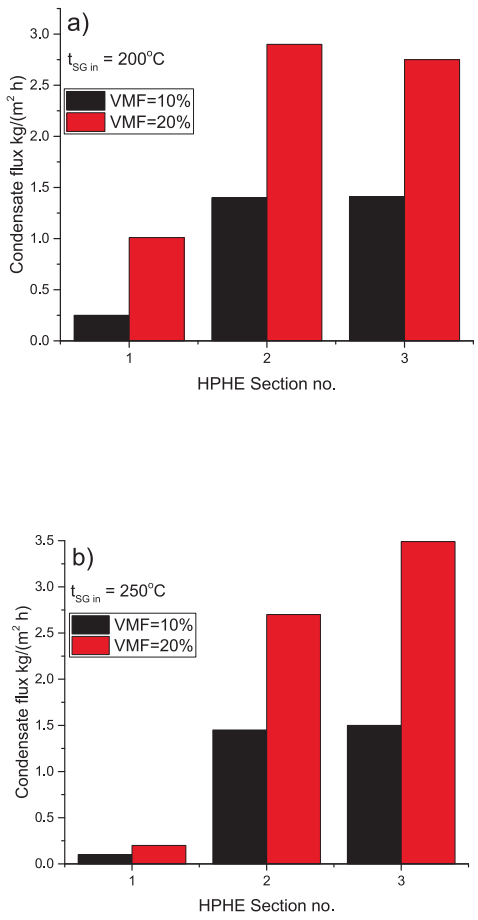

Fig. 16. Typical distribution of condensate flux from condensation unit sections in the case of different VMF and simulated gas inlet temperatures of 200 °C (a) and 250 °C (b).

decrease in the condensate flux. In general, at a higher simulated gas inlet temperature (Fig. 16b), the condensate flux was increasing along the condensation unit sections, while at a lower simulated gas inlet temperature, the condensation rate was almost stable in sections no. 2 and no. 3. According to the acid dew point diagram, condensation of HCl was expected in section no. 1. As such during the experiments, the condensate (Fig. 17) from section no. 1 (Monel 400) was green, while from section no. 2 or 3 it was slightly green and / or colorless.

As expected, a high liquid density was measured in the condensate collected in section no. 1 where the HCl concentration was up to 30%, while in sections no. 2 and 3 the concentration was very diluted (0–2%).

Fig. 17. Typical condensate color in the case of pipe made of Monel 400.

Due to a rather high HCl concentration in the condensate from section no. 1 and green coloring of the liquid, the presence of corrosion products here is highly probable. Therefore, this result is in line with the lab scale results for the HCl liquid phase corrosion of Monel 400 where a significant amount of chlorides were formed (4.2 wt% Cl). Thus, the formation of deposits of $CuCl_2xH_2O$ and $NiCl_2xH_2O$, both soluble and green, is expected by the vapor phase and HCl-rich condensate (liquid phase) corrosion. These corrosion layer deposits on the surface of the Monel 400 pipes are readily soluble in the highly acidic condensate film formed and were eventually collected in the tanks as a green solution.

In Fig. 18, the view of the condensation unit with the removed side covers before experiments is shown. As indicated above, the gas side walls, top and bottom of the heat exchanger were made of Monel 400 and stainless steel in sections no. 2 and 3.

After 50 h of testing under HCl acid injection, the condensation unit internal horizontal and vertical surfaces were covered with green sediments. A larger quantity of sediments was located on the bottom plate of the condensation unit (Fig. 19). The deposits were not firmly attached and were easily removable by hand.

In Monel 400 pipes, layers of brown glossy deposits were observed along with green sediments. This was especially true for all the pipes at inlet, while towards the end of the row in this section, green deposits were predominant (Fig. 19). Both copper and nickel chlorides appear in such colors. The monoclinic anhydrous $CuCl_2$ is yellowish-brown and is found when no moisture is available, as expected in the early and higher temperature condensation stage of the condensation unit. In more humid conditions, this substance forms the orthorhombic blue-green dihydrate $CuCl_2{\cdot}2H_2O$, with two water molecules of hydration. Also, the nickel chloride appears yellow–brown when water is absent and green in its hydrated form.

After removing the corrosion deposits from pipes in section no. 1 with a wet sponge (Fig. 20), visual inspection revealed that the pipe surfaces were no longer as glossy as before installation but mostly matte, indicating corrosion in a similar way as discussed in the previous section of the lab scale testing.

Collected surface deposits from the pipe specimens in section no. 1 are shown in Fig. 21.

The amount of iron in the deposits from the pipes and the amount of the deposits collected from the bottom plate around section no. 1 (Fig. 22) was low (<4%). The results also show that the prevailing chemical elements are copper, nickel, aluminum, and chlorine. These results are in line with what was observed in the liquid phase corrosion during the lab testing. However, in this case, both vapor and liquid phase corrosion occurred as Monel 400 specimens encountered HCl acid vapor and then a condensation film of concentrated HCl solution. The high concentration of oxygen in the corrosion deposit is indicative. The presence of aluminum (Al) in the corrosion deposits, though minor,

Fig. 18. Internal surfaces of the condensation unit before experiments.

Fig. 19. Internal surfaces of the condensation unit after experiments.

Fig. 20. Monel 400 pipes after cleaning (only pipes marked with red dots were cleaned) in condensation unit section no. 1. (For interpretation of the references to colour in this figure legend, the reader is referred to the web version of this article.)

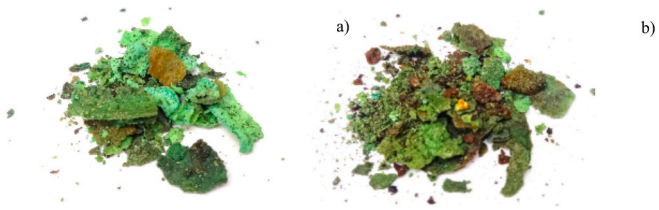

Fig. 21. Sediments collected from the pipes surfaces of section no. 1 (a) and from the bottom plate of the condensation unit (b).

suggests potential contamination or environmental interaction, though its role in corrosion resistance remains a matter of future study.

Solid sediments collected from the bottom plate around pipes in section no. 1 showed lower copper, iron, and aluminum concentrations;

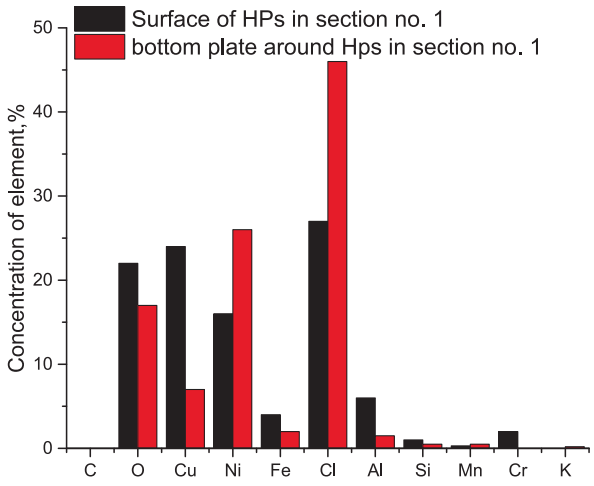

Fig. 22. Concentrations of chemical elements of solid sediments (wt, %) from the surface of pipes in section no. 1, from the bottom plate around Monel 400 pipes in section no. 1 (thin lines indicate standard deviation; if lines are not indicated, this means that standard deviation is less than 1%).

however, nickel concentration was higher by a factor of 1.6 (Fig. 22) in comparison to that obtained from the surface of pipes. The chlorine accumulation in the bottom plate solid sediments around pipes in section no. 1 was also the largest (Fig. 23), indicating the dissolution effect of the acidic condensate on the corrosion layer deposit on the Monel 400 tubes, thus, primarily accumulating soluble corrosion products or loosely adherent particles that are readily susceptible to erosion. On the other hand, possibly existing nickel oxide formations on Monel 400 are not soluble in an HCl-rich condensate.

The surface morphology of the corrosion layer deposit is presented in Fig. 23 both from the surface of pipes in section no. 1 as well as from the corresponding bottom plate. The deposits are highly porous, with the corrosion products on the specimens exhibiting a loose structure and large voids, as if they have been partially dislodged or eroded by flow-induced chemical dissolution forces. The corresponding deposits on the bottom plate seem more uniform and concrete with smaller pores and cracks.

3.4. Discussion on corrosion findings

The corrosion mechanisms of Monel 400 in hydrofluoric acid (HF) and hydrochloric acid (HCl) mixtures reveal a complex interaction between fluoride and chloride ions, leading to accelerated degradation compared to individual acid exposure. In pure HF solutions, Monel 400 exhibits a degree of passivation due to the formation of a protective layer comprising Cu_2O and NiO, which limits further corrosion. However, fluoride ions, known for their ability to penetrate passive films, gradually weaken this protective layer, leading to increased dissolution of the alloy. Electrochemical results indicate that corrosion rates increase significantly when HF and HCl are combined, highlighting the role of chloride ions in breaking down protective oxides. Chloride ions disrupt passivation and facilitate the formation of soluble metal chlorides, such as $NiCl_2$ and $CuCl_2$, which readily dissolve and expose fresh metal surfaces to a continued attack. In vapor-phase conditions, the corrosion rate is ten to twenty times higher than in liquid HF, as chloride ions in the gaseous phase enhance the aggressive attack by preventing repassivation. Additionally, the presence of oxidizing species, such as oxygen (O_2), Cu^{2+}, and Fe^{3+} ions, further increases corrosion by accelerating metal dissolution and facilitating localized attack. The combination of fluoride and chloride ions, particularly in HF-HCl vapor, represents the most severe environment, where both acids synergistically lead to aggressive material loss, without excluding localized pitting, and the formation of CuF_2 and NiF_2, which are known to play a critical role in

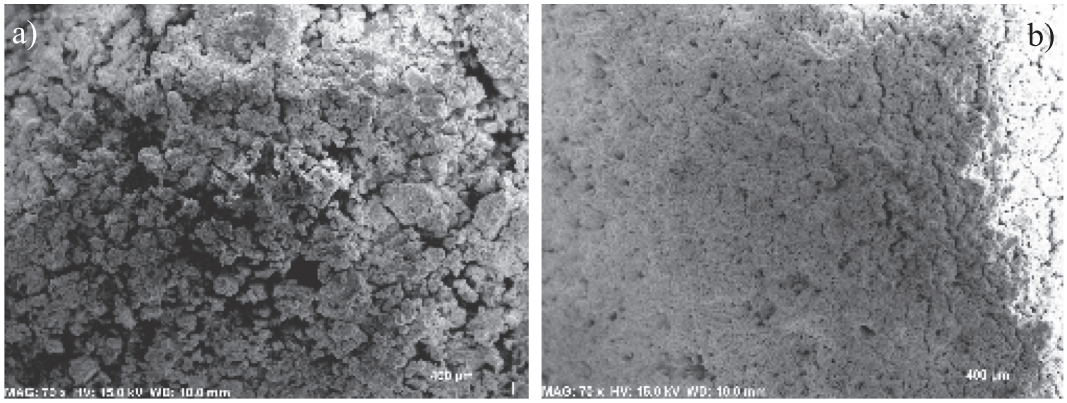

Fig. 23. SEM images of corrosion deposits: surface of pipe in section no. 1 (a), from the bottom plate in section no. 1 (b).

stress corrosion cracking.

The lab scale findings correlate strongly with failures observed in upscale tests in a condensation unit for Monel 400 components exposed to an HCl environment. The Monel 400 tubes experienced severe corrosion, particularly in sections where acidic vapors condensed. In this environment specimens encounter the corrosion mechanisms of both vapor and liquid phase (after condensation occurs). The electrochemical data indicate that liquid-phase corrosion in HCl environments results in accelerated material degradation, explaining why the first rows of the specimens in the industrial setting showed the most severe damage. The green and brown corrosion deposits found on them align with the laboratory observations of $NiCl_2{\cdot}xH2O$ and $CuCl_2{\cdot}xH2O$ formation, which have been linked to localized corrosion and passivation failure. Moreover, SEM/EDX analysis confirms that chlorine rich deposits are responsible for the accelerated breakdown of Monel 400. The industrial level failure is attributed to operating conditions that promote a combination of acid vapor and acid condensate attack in high temperatures that accelerate corrosion rates, and the presence of oxidizing species, such as Fe^{3+} and Cu^{2+} ions either as impurities or as corrosion products, which catalyze material degradation. The findings suggest that improper material selection and lack of protective coatings contributed to the premature failure of the engineering alloys, highlighting the need for more resistant materials or corrosion inhibitors in such environments.

The experimental findings align with prior literature on Monel 400 corrosion in HF and HCl, reinforcing the understanding that fluoride ions weaken passive films, while chloride ions actively disrupt protective layers. Studies by Dai et al. [15] and Guo et al. [25] reported that Monel 400 undergoes passivation failure in HF vapor, leading to high corrosion rates exceeding 4.5 mm/y, similar to the severe material loss observed in HF-HCl vapor-phase tests. The synergistic effect of HF and HCl is also well-documented in API RP 751, where industrial failures in alkylation processes were linked to chloride-induced passivity breakdown in nickel-based alloys. However, unlike some literature findings that suggest Monel 400 has superior resistance in HF environments [18,19,34,37,41], the present study demonstrates that under oxidizing and chloride-rich conditions, corrosion rates exceed expected values, with CuF_2 formation leading to stress corrosion cracking (SCC). This confirms that while Monel 400 performs well in pure HF, its resistance diminishes significantly when chloride ions and oxidizing agents are introduced.

4. Conclusions and recommendations

The study highlights the severe corrosion mechanisms affecting Monel 400 in HF-HCl mixtures, particularly in vapor-phase environments where corrosion rates increase drastically due to the synergistic attack of fluoride and chloride ions. The industrial-level case study confirms that similar degradation patterns observed in laboratory tests were responsible for the failure of Monel 400 specimens in the condensation unit system handling corrosive acid vapors. Key findings suggest that chloride ions play a crucial role in disrupting passive films, leading to localized attack and increased material dissolution.

Regarding industry implications, material selection must account for synergistic HF-HCl corrosion effects. While Monel 400 is resistant to pure HF, its performance degrades significantly in mixed HF-HCl environments. Furthermore, herein we indicate that vapor-phase corrosion is significantly more aggressive than liquid-phase corrosion, which implies that industrial designs must incorporate special measures when handling processes with acid vapors combined with acid condensation on metal surfaces. The presence of oxidizing agents (O_2, Fe^{3+}, Cu^{2+}) also amplifies corrosion rates, and as a result industrial systems must minimize exposure to oxidizing species to enhance alloy durability.

As recommendations for corrosion mitigation, alternative materials should be used for HF and HCl mixtures: alloys such as Hastelloy C-276 (Ni-Cr-Mo) or Inconel 625 (Ni-Cr-Mo-Nb) exhibit superior resistance to HF and HCl mixtures. Protective coatings such as fluoropolymer or ceramic barriers should be applied in order to mitigate direct acid-metal interactions and reduce corrosion rates. As an additional measure, environmental controls should be implemented: controlling oxygen ingress and reducing Fe^{3+} and Cu^{2+} contamination can significantly slow corrosion. Finally, designs should control acid condensation: engineering solutions such as inert gas purging, can help prevent acid filmwise formation on critical surfaces or limit its residence time through surface engineering which induces hydrophobicity [19,58–61].

By adopting these strategies, industries operating in HF-HCl environments can extend equipment lifespan, reduce maintenance costs, and prevent catastrophic failures, ensuring a safer and more efficient operation of industrial systems.

CRediT authorship contribution statement

Vassilis Stathopoulos: Writing – review & editing, Project administration, Methodology, Funding acquisition, Conceptualization. **Pavlos K. Pandis:** Writing – original draft, Visualization, Investigation. **Athanasios Zarkadoulas:** Writing – original draft, Visualization, Investigation. **Paraskevi Nanou:** Visualization, Investigation. **Dimitrios Fragkoulis:** Investigation. **Robertas Poškas:** Validation, Resources. **Arūnas Sirvydas:** Visualization, Investigation. **Povilas Poškas:** Supervision. **Jurgis Jankaukas:** Investigation. **Hussam Jouhara:** Writing – review & editing, Project administration, Funding acquisition.

Declaration of competing interest

The authors declare that they have no known competing financial interests or personal relationships that could have appeared to influence the work reported in this paper.

Acknowledgements

This work has received funding from the European Union's Horizon 2020 Research and Innovation Programme under Grant Agreement No 958274.

Data availability

Data will be made available on request.

References

[1] V. Stathopoulos, V. Sadykov, S. Pavlova, Y. Bespalko, Y. Fedorova, L. Bobrova, A. Salanov, A. Ishchenko, V. Stoyanovsky, T. Larina, V. Ulianitsky, Z. Vinokurov, V. Kriventsov, Design of functionally graded multilayer thermal barrier coatings for gas turbine application, Surf. Coat. Technol. 295 (2016) 20–28.
[2] R. Singh, 9 - Nonferrous materials, in: R. Singh (Ed.), Applied Welding Engineering (Third Edition), Butterworth-Heinemann, 2020, pp. 85–91.
[3] G. Chliveros, I. Tzanetatos, K. Kamzelis, MaVeCoDD dataset: marine vessel hull corrosion in dry-dock images, Mendeley Data 1 (2021) 1–8.
[4] G. Chliveros, S.V. Kontomaris, A. Letsios, Automatic identification of corrosion in marine vessels using decision-tree imaging hierarchies, in: Eng, Vol. 4, 2023, pp. 2090-2099.
[5] A.K. Parida, K. Maity, Comparison the machinability of Inconel 718, Inconel 625 and Monel 400 in hot turning operation, Eng. Sci. Technol., An Int. J. 21 (2018) 364–370.
[6] A.K. Parida, K. Maity, Experimental investigation on tool life and chip morphology in hot machining of Monel-400, Eng. Sci. Technol., An Int. J. 21 (2018) 371–379.
[7] ISO 8044:2024(en) Corrosion of metals and alloys — Basic terms and definitions, (2024).
[8] G. Koch, J. Varney, N. Thompson, O. Moghissi, M. Gould, J. Payer, International measures of prevention, application, and economics of corrosion technologies study, in, NACE International, Houston, 2012.
[9] M.A. Jafar Mazumder, Global impact of corrosion: occurrence, cost and mitigation, Global J. Eng. Sci. 5 (2020).
[10] V. Kovalenko, V. Kotok, V.N. Stathopoulos, Smart coatings against corrosion, in: A.-G. Olabi (Ed.), Encyclopedia of Smart Materials, Elsevier, Oxford, 2022, pp. 400–413.
[11] P. Pandis, E. Xenogiannopoulou, P. Sakkas, G. Sourkouni, C. Argirusis, V. Stathopoulos, Compositional effect of Cr contamination susceptibility of La 9.83 Si 6–x− y Al x Fe y O 26±δ apatite-type SOFC electrolytes in contact with CROFER 22 APU, RSC Adv. 6 (2016) 49429–49435.
[12] iWAYS Project - Innovative WAter recoverY solutions through recycling of heat, materials and water across multiple sectors - Available at: https://www.iways.eu/; European Commission, CORDIS, Project 958274. Available at: https://cordis.europa.eu/project/id/958274 (accessed January 2026).
[13] United Nations, Sustainable Development Goals. Available at: https://sdgs.un.org/goals (accessed January 2026).
[14] L. Montorsi, M. Venturelli, B. Delpech, H. Jouhara, IWAYS - recycling of heat, water and material across multiple sectors: ceramic, chemical and steel industry, Adv. Sci. Technol. 133 (2023) 55–63.
[15] H. Dai, S. Shi, L. Yang, C. Guo, X. Chen, Recent progress on the corrosion behavior of metallic materials in HF solution, Corros. Rev. 39 (2021) 313–337.
[16] H. Dai, S. Shi, L. Yang, J. Hu, C. Liu, C. Guo, X. Chen, Effects of elemental composition and microstructure inhomogeneity on the corrosion behavior of nickel-based alloys in hydrofluoric acid solution, Corros. Sci. 176 (2020) 108917.
[17] S.J. Pawe, Corrosion of high-alloy materials in aqueous hydrofluoric acid environments, Corrosion 50 (1994) 963–971.
[18] Corrosion Resistance of Nickel-containing alloys in Hydrofluoric Acid, Hydrogen Fluride and Fluorine (CEB-5), A practical Guide to the use of Nickel-containing Alloys No 443, Nickel Insitute, (1976).
[19] H.S. Jennings, Materials for hydrofluoric acid service in the new millennium, Corrosion 2001 (2001). NACE-01345.
[20] K.H. Kim, S.H. Lee, N.D. Nam, J.G. Kim, Effect of cobalt on the corrosion resistance of low alloy steel in sulfuric acid solution, Corros. Sci. 53 (2011) 3576–3587.
[21] A. Ravi Shankar, U. Kamachi Mudali, Refractory metal coatings on titanium to improve corrosion resistance in nitric acid medium, Surf. Coat. Technol. 235 (2013) 155–164.
[22] D. Daoud, T. Douadi, S. Issaadi, S. Chafaa, Adsorption and corrosion inhibition of new synthesized thiophene Schiff base on mild steel X52 in HCl and H2SO4 solutions, Corros. Sci. 79 (2014) 50–58.
[23] B. Liu, X. Wei, W. Wang, J. Lu, J. Ding, Corrosion behavior of Ni-based alloys in molten NaCl-CaCl2-MgCl2 eutectic salt for concentrating solar power, Sol. Energy Mater. Sol. Cells 170 (2017) 77–86.
[24] H. Sun, P. Zhang, J. Wang, Effects of alloying elements on the corrosion behavior of Ni-based alloys in molten NaCl-KCl-MgCl2 salt at different temperatures, Corros. Sci. 143 (2018) 187–199.
[25] L. Guo, Q. Liu, H. Yin, T.J. Pan, Z. Tang, Excellent corrosion resistance of 316 stainless steel in purified NaCl-MgCl2 eutectic salt at high temperature, Corros. Sci. 166 (2020) 108473.
[26] B. Löchel, H.H. Strehblow, Breakdown of passivity of iron by fluoride, Electrochim. Acta 28 (1983) 565–571.
[27] R.B. Rebak, J.R. Dillman, P. Crook, C.V.V. Shawber, Corrosion behavior of nickel alloys in wet hydrofluoric acid, Mater. Corros. 52 (2001) 289–297.
[28] P.E. Osborne, A. S. Icenhour, G.D.D. Cul, Hydrofluoric acid corrosion study of high-alloy materials, in: N.S.a.T. Division (ed.), OAK RIDGE NATIONAL LABORATORY, U.S. DEPARTMENT OF ENERGY, 2002.
[29] P. Crook, N. S. Meck, R.B. Rebak, The influence of composition upon surface degradation and stress corrosion cracking of the Ni-Cr-Mo alloys in wet hydrofluoric acid, in: Corrosion/2007 Conference and Exposition, Nashville, TN, United States, 2006.
[30] Y. Li, X. Fan, N. Tang, H. Bian, Y. Hou, Y. Koizumi, A. Chiba, Effects of partially substituting cobalt for nickel on the corrosion resistance of a Ni–16Cr–15Mo alloy to aqueous hydrofluoric acid, Corros. Sci. 78 (2014) 101–110.
[31] Y. Hou, Y. Li, F. Wang, C. Zhang, Y. Koizumi, A. Chiba, Influence of Mo concentration on corrosion resistance to HF acid solution of Ni–Co–Cr–Mo alloys with and without Cu, Corros. Sci. 99 (2015) 185–193.
[32] B. Yang, Y. Hou, Q. Lei, Y. Li, A. Chiba, Influence of Cu addition on corrosion behavior and tensile performance of Ni-30Co-16Cr-15Mo-6Fe alloy, Mater Charact 161 (2020) 110140.
[33] B. Yang, Y. Hou, Y. Li, A. Chiba, Roles of Mo and Cu on electrochemical behaviors of Ni-base alloys in hydrofluoric acid solution, J. Electrochem. Soc. 167 (2020) 101502.
[34] H.R. Copson, C.F. Cheng, Stress corrosion cracking of monel in hydrofluoric acid, Corrosion 12 (1956) 71–77.
[35] W.J. Braun, F.W. Fink, G.L. Ericson, The corrosion on Monel and 70-30 cupronickel in hydrofluric acid, Report No. BMI-1237 UC-25 Metallurgy and Ceramics (TID-4500, 13th Ed. , Suppl.), Batelle Memorial Insitute, Columbus 1, Ohio (1957).
[36] R. Kumar, U. Chatterjee, Prevention possibilities of stress corrosion cracking of Monel 400 in hydrofluoric acid. 11th International Conference on Fracture, 2005.
[37] C. Guo, S. Shi, H. Dai, X. Sun, J. Yu, X. Chen, The deterioration effects of corrosion product deposition on Ni-Cu alloy in hydrofluoric acid vapor phase, Corros. Sci. 219 (2023) 111256.
[38] H. Dai, S. Shi, J. Tang, C. Guo, Z. Ning, X. Chen, Revealing the effect of heat treatment on stress corrosion cracking behavior of Monel 400 alloy in hydrofluoric acid vapor environment, Corros. Sci. 215 (2023) 111046.
[39] R.B. Rebak, Stress corrosion cracking (SCC) of nickel-based alloys, Editor(s): V.S. Raja, Tetsuo Shoji, In Woodhead Publishing Series in Metals and Surface Engineering, Stress Corrosion Cracking, Woodhead Publishing, 2011, Pages 273-306, ISBN 9781845696733, https://doi.org/10.1533/9780857093769.3.273.
[40] M. Schussler, Metal materials for handling aqueous hydrofluoric acid, Indus. Eng. Chem. 47 (1955) 133–139.
[41] H. Pray, F. Fink, B. Friedl, W. Braun, Corrosion-resistant materials for hydrofluoric acid: progress Report, University of North Texas Libraries, Columbus, Ohio, 1953.
[42] V.L. Graph, W. Wittich, Untersuchung von Sonderfällen der Spannungskorrosion bei homogenen, nicht übersättigten Mischkristallen und der hierbei auftretenden elektrochemischen Prozesse, Mater. Corros. 17 (1966) 385–405.
[43] L.G. Everhart, Stress corrosion cracking, in: Faculty of the Graduate College of Vol. MSc, Oklahoma State University, Oklahoma, 1987.
[44] H. Dai, S. Shi, C. Guo, Z. Ning, Y. Kuang, X. Chen, The synergistic effect between fluoridation degradation and dislocation sliding on stress corrosion failure of Monel 400 alloy in HF vapor, Corros. Sci. 224 (2023) 111489.
[45] D.D.C. Williams, A. Shaik, E. Li, K. Li, K.L. Moore, R.C. Newman, Dealloying of Monel 400 in nuclear steam generators, Corros. Sci. 251 (2025) 112909.
[46] A.M. Shams El Din, M.E. El Dahshan, A.M. Taj El Din, Dissolution of copper and copper-nickel alloys in aerated dilute HCl solutions, Desalination 130 (2000) 89–97.
[47] M. Davies, Alloy selection for service in chlorine, hydrogen chloride and hydrochloric acid-a guide to the use of nickel-containing alloys, Nickel Institute, 2022.
[48] A. Bahadori, Chapter 15 - corrosion in pipelines and piping systems, in: A. Bahadori (Ed.), Oil and Gas Pipelines and Piping Systems, Gulf Professional Publishing, Boston, 2017, pp. 395–481.
[49] Z.B. Wang, H.X. Hu, Y.G. Zheng, Synergistic effects of fluoride and chloride on general corrosion behavior of AISI 316 stainless steel and pure titanium in H2SO4 solutions, Corros. Sci. 130 (2018) 203–217.
[50] G. Kear, B.D. Barker, K. Stokes, F.C. Walsh, Electrochemical corrosion behaviour of 90—10 Cu—Ni alloy in chloride-based electrolytes, J. Appl. Electrochem. 34 (2004) 659–669.
[51] J. Mathiyarasu, N. Palaniswamy, V.S. Muralidharan, An insight into the passivation of cupronickel alloys in chloride environment, J. Chem. Sci. 113 (2001) 63–76.
[52] C. Nyby, X. Guo, J.E. Saal, S.-C. Chien, A.Y. Gerard, H. Ke, T. Li, P. Lu, C. Oberdorfer, S. Sahu, S. Li, C.D. Taylor, W. Windl, J.R. Scully, G.S. Frankel, Electrochemical metrics for corrosion resistant alloys, Sci. Data 8 (2021) 58.
[53] A. Raveendran, M. Chandran, R. Dhanusuraman, A comprehensive review on the electrochemical parameters and recent material development of electrochemical water splitting electrocatalysts, RSC Adv. 13 (2023) 3843–3876.
[54] A. Kraš, I. Milošev, Comparative electrochemical and thermodynamic study of cold-rolled steel, Al alloy AA5754, and Zn corrosion in fluoride and chloride solutions, Electrochim. Acta 502 (2024) 144819.
[55] C.J. Semino, P. Pedeferri, G.T. Burstein, T.P. Hoar, The localized corrosion of resistant alloys in chloride solutions, Corros. Sci. 19 (1979) 1069–1078.
[56] C. Guo, S. Shi, H. Dai, J. Yu, X. Chen, Corrosion mechanisms of nickel-based alloys in chloride-containing hydrofluoric acid solution, Eng. Fail. Anal. 140 (2022) 106580.
[57] F. Verhoff, B. jt,, Predicting dew points of flue gases, Chem. Eng. Progress 70 (1974) 71–72.

[58] P. Nanou, A. Zarkadoulas, P.K. Pandis, I. Tsilikas, I. Katis, D. Almpani, N. Orfanoudakis, N. Vourdas, V. Stathopoulos, Inducing hydrophobicity in Stainless Steel 304 by mechanical texturing and chemical functionalization, Int. J. Adv. Manuf. Technol. 133 (2024) 307–319, https://doi.org/10.1007/s00170-024-13701-w.

[59] P. Nanou, A. Zarkadoulas, P.K. Pandis, I. Tsilikas, I. Katis, D. Almpani, N. Orfanoudakis, N. Vourdas, V.N. Stathopoulos, Micromachining on stainless steel 304 for improved water condensation properties, Key Eng. Mater. 962 (2023) 19–26.

[60] P. Nanou, J. Konstantaras, A. Zarkadoulas, P.K. Pandis, N. Vourdas, V. N. Stathopoulos, Construction, evaluation, and performance of a water condensation test unit, Key Eng. Mater. 133 (2023) 35–43.

[61] I. Iliopoulos, A. Karampekios, P.K. Pandis, N. Vourdas, H. Jouhara, S. Tassou, V. N. Stathopoulos, Evaluation of organic coatings for corrosion protection of condensing economizers, Procedia Struct. Integrity 10 (2018) 295–302.